Nano Research

Open Access

Research Article

Gut probiotic *Akkermansia muciniphila*-derived extracellular vesicles deliver miR-21-5p to alleviate atopic dermatitis by targeting TLR4 signaling

Juan Wang[1,2,§] ✉, Yanyan Zhang[1,2,§], Siqi Yuan[1,2,§], Mengting Zhang[3], Xiuwen Zhang[3], Jing Chen[1,2], Hanyu Dou[1,2], Hua Cheng[4] ✉, and Xiaolei Ding[1,2] ✉

[1] *Institute of Geriatrics (Shanghai University), Affiliated Nantong Hospital of Shanghai University (The Sixth People's Hospital of Nantong), School of Medicine, Shanghai University, Nantong 226011, China*
[2] *Shanghai Engineering Research Center of Organ Repair, School of Medicine, Shanghai University, Shanghai 200444, China*
[3] *Eye & ENT Hospital, Fudan University, Shanghai 200031, China*
[4] *Massachusetts General Hospital, Harvard Medical School, Charlestown, MA 02129, USA*
[§] *Juan Wang, Yanyan Zhang, and Siqi Yuan contributed equally to this work.*

Cite this article: *Nano Research*, **2026**, *19*, 94908421. https://doi.org/10.26599/NR.2026.94908421

ABSTRACT: Atopic dermatitis (AD), a prevalent chronic inflammatory skin disorder, severely impairs patients' quality of life. Mounting evidence indicates that gut microbiomes regulate AD pathogenesis through the gut-skin axis; yet the therapeutic potential of gut microbiomes-derived extracellular vesicles (EVs) remains largely unexplored. Here, we isolated EVs from gut probiotic *Akkermansia muciniphila* (AKK-EVs) and evaluated their therapeutic efficacy and underlying mechanisms against AD pathogenesis. AKK-EVs exhibited pronounced anti-inflammatory and antioxidant properties *in vitro*. MicroRNA profiling revealed that miR-21-5p was highly enriched within AKK-EVs and critically mediated their biological activity. Mechanistically, miR-21-5p directly targeted *TLR4* gene, thereby suppressing NF-κB signaling pathway and downstream proinflammatory cytokine production. Notably, AKK-EVs exhibited excellent stability in gastrointestinal condition, and upon oral administration, preferentially homed to inflamed skin tissues via the gut-skin axis.Both oral and subcutaneous administration of AKK-EVs alleviated AD-like phenotypes, reshaped the inflammatory microenvironment and restored compromised skin barrier. Collectively, this study uncovers a previously unrecognized role of AKK-EVs in modulating AD and highlights probiotic-derived EVs as a promising therapeutic strategy for inflammatory skin disorders.

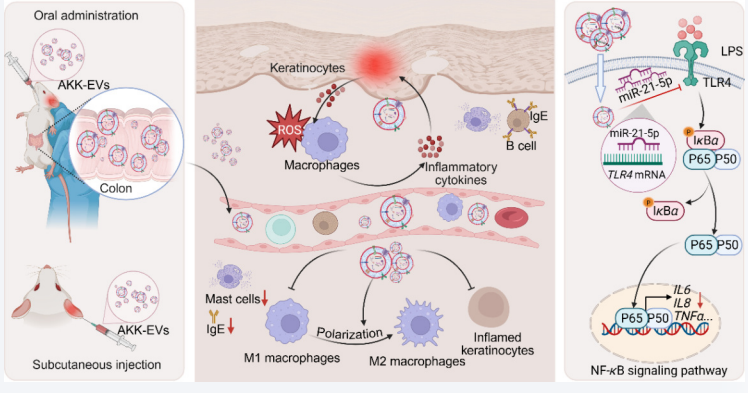

KEYWORDS: extracellular vesicle, *Akkermansia muciniphila*, atopic dermatitis, microRNA, inflammation, toll-like receptor 4 (TLR4)

1 Introduction

Atopic dermatitis (AD) is one of the most common chronic inflammatory skin disorders, affecting approximately 15% of children and up to 10% of adults worldwide [1]. AD is characterized by pruritus, recurrent eczematous lesions, pain and even anxiety-related symptoms in the most severe cases [2]. The pathogenesis of AD is complex and multifactorial, involving genetic factors, compromised skin barrier function, dysregulated immune responses and abnormal microbiome [2]. Clinically, conventional therapies for AD, such as topical glucocorticoids, antihistamines, and systemic immunosuppressants can alleviate symptoms but are frequently associated with adverse effects and high relapse rates [3]. Recent advances in the understanding of AD pathogenesis have led to the identification of novel molecular targets and the development

Received: November 27, 2025; **Revised:** January 6, 2026
Accepted: January 8, 2026

✉Address correspondence to Juan Wang, Juanw@shu.edu.cn; Xiaolei Ding, xlding@shu.edu.cn; Hua Cheng, hcheng9@mgh.harvard.edu

of first-in-class biologics and small-molecule inhibitors for moderate to severe diseases. Nevertheless, AD remains an unpredictable and relapsing condition, and the long-term safety and efficacy of existing treatments are still of concern. Consequently, there is an unmet clinical need for developing safe and efficacious strategies to manage AD.

Gut microbiomes are increasingly recognized as a critical regulator of both local and systemic physiology, influencing distant organs such as the skin, brain, and liver [4–7]. In recent years, the interaction of the gut microbiome and skin homeostasis has emerged as a pivotal area of research, giving rise the concept of the gut-skin axis [8–10]. Supporting this, several independent studies have revealed distinct alterations in the gut microbiome composition of AD patients compared to healthy individuals [11–13]. As a result, gut probiotics and their metabolites have emerged as promising candidates for the treatment and prevention of AD [9, 14, 15]. Their beneficial effects are attributed to the modulation of inflammatory responses, enhancement of intestinal barrier function, and restoration of gut microbiota diversity. For example, oral administration of *Lactobacillus paracasei* KBL382, a gut probiotic, changed the composition of gut microbiota and modulated the immune responses, thereby relieving AD-like symptoms in mice [16]. Furthermore, fecal microbiota transplant has also shown therapeutic potential in AD [17]. However, the therapeutic application of live bacteria is limited by safety concerns, particularly in immunocompromised individuals, and their inherent poor stability within the gastrointestinal microenvironment.

Extracellular vesicles (EVs) are nanosized, membrane-enclosed particles secreted by virtually all cell types, including mammalian cells and bacteria [18–21]. EVs contain abundant bioactive materials, such as microRNAs (miRNAs), proteins, and lipids, which can be transported to target cells, thereby regulating multiple biological processes, such as cell inflammation and metabolism [22, 23]. Recent studies have increasingly focused on the therapeutic potential of EVs derived from bacteria, owing to their cost-effectiveness, safety, high target specificity, and superior stability [9, 24–26]. For example, EVs produced by gut bacteria *Parabacteroides goldsteinii* can specifically circulate to inflamed skin to alleviate psoriasis [24]. Our recent work demonstrated that gut probiotic *Lactobacillus rhamnosus* GG-derived EVs facilitated cutaneous wound healing by regulating the re-epithelialization and angiogenesis with a high safety profile [25]. Collectively, these findings highlight the promise of bacterial EVs (BEVs) as a novel and promising strategy to overcome the challenges associated with conventional glucocorticoids and live bacterial therapeutics.

Akkermansia muciniphila (AKK) is a probiotic commonly found in the mammalian gut [27]. A decreased abundance of AKK has been reported in patients with AD [28, 29]. Notably, AKK supplementation confers multiple health benefits, including the amelioration of AD symptoms, modulation of immune responses, tumor suppression, and maintenance of intestinal homeostasis [28, 30, 31]. However, whether and how EVs derived from AKK (AKK-EVs) modulate AD pathogenesis remain unexplored. In this study, we isolated AKK-EVs and assessed their anti-inflammatory and antioxidant efficacy *in vitro*. We further performed transcriptomic profiling to identify key miRNAs within AKK-EVs and explored their regulatory effects on inflammatory signaling pathways implicated in AD. Using a 2,4-dinitrofluorobenzene (DNFB)-induced AD mouse model, we evaluated the bio-distribution, safety, and therapeutic efficacy of AKK-EVs following both oral and topical administration. Our findings reveal a previously unrecognized function of gut probiotic-derived EVs and propose AKK-EVs as a safe and innovative therapeutic strategy for inflammatory skin diseases.

2 Experimental

2.1 Isolation and characterization of AKK-EVs

AKK (ATCC BAA-835) was cultured in brain heart infusion (BHI) broth (Hopebio, HB8297-1) supplemented with 0.05% L-cysteine under anaerobic conditions [32]. The isolation of AKK-EVs was performed as previously described, in compliance with the Minimal Information for Studies of Extracellular Vesicles (MISEV2023) guidelines [33, 34]. Briefly, after 4 days of culture, the supernatant of AKK was collected by centrifugation at 4000*g* for 10 min. It was then centrifuged at 10,000*g* for 15 min and filtered through a 0.22 μm filter to get rid of the bacterial debris and large particles. Subsequently, the supernatant was ultra-centrifuged at 150,000*g* for 2 h at 4 °C, and the sediments were resuspended with phosphate-buffered saline (PBS) followed by a second ultracentrifugation at 150,000*g* for 2 h at 4 °C. The resulting EVs-enriched fractions were resuspended in sterile PBS and stored at −80 °C or used immediately. The morphology and particle size of AKK-EVs were assessed using transmission electron microscopy (TEM, Hitachi, Japan) and nanoparticle tracking analysis (NTA, ZetaView, Germany), respectively. Dynamic light scattering (Zetasizer Nano ZS90, Malvern) was used for zeta-potential analysis.

To characterize RNA cargo of AKK-EVs, the total RNA was extracted with Trizol and analyzed on a 5% agarose gel. To characterize the protein cargo of AKK-EVs, total protein was separated on a 12% sodium dodecyl sulfate-polyacrylamide gel electrophoresis (SDS-PAGE) gel and stained with Coomassie brilliant blue for 2 h. After destaining, the gel was imaged using a gel documentation system.

2.2 Cells and cell culture

Human keratinocyte cell line HaCaT and mouse macrophage cell line RAW264.7 were obtained from the Cell Bank of the Chinese Academy of Science (Shanghai, China). Cells were maintained in Dulbecco's modified Eagle's medium (DMEM, Thermo Fisher Scientific) composed of 10% fetal bovine serum (FBS) and 1% Penicillin/Streptomycin. Cultures were incubated in the humidified incubator with 5% CO_2 at 37 °C. Cells within 7 passages were used for all experiments.

2.3 Cell viability

HaCaT and RAW264.7 cells were seeded in 96-well plates at a density of 7×10^3 cells per well. After 24 h, cells were treated with various concentrations of AKK-EVs for 24 h. Subsequently, 10 μL of cell counting kit 8 (CCK8) reagent (Meilunbio, MA0218) was added to each well and incubated for another 2 h at 37 °C. The absorbance was detected at 450 nm using a microplate reader (Infinite e plex, Tecan, Austria). Wells without cells served as blank. Cell viability was calculated according to the following formula: $(A450_{treated} - A450_{blank})/(A450_{Control} - A450_{blank})$, where A450 indicates absorbtance at the wavelength of 450 nm.

2.4 Cellular uptake assay

AKK-EVs were labeled with red fluorescence dye Vybrant™ DID (Invitrogen, V22887) as previously described [35]. Unincorporated dyes were removed by washing three times with PBS at 4 °C. HaCaT and RAW264.7 cells were then treated with DID (1,1'-dioctadecyl-3,3,3',3'-tetramethylindodicarbocyanine perchlorate)-labeled AKK-EVs for 0, 2, 6 or 12 h. Subsequently, cells were fixed with 4% paraformaldehyde (PFA) and stained with 4',6-diamidino-2-phenylindole (DAPI) to visualize nuclei. Fluorescence images were captured using a confocal fluorescence microscope (KEYENCE, BZ-X810).

2.5 Quantitative real-time polymerase chain reaction (qRT-PCR)

Total RNA was extracted using TRIzol reagent (Invitrogen) according to the manufacturer's instructions. For mRNA analysis, genomic DNA was removed by DNase I treatment, and complementary DNA (cDNA) was synthesized using a reverse transcription kit (Vazyme, R323-01). SYBR Green (Vazyme, Q711-02) was used in the qRT-PCR analysis of cDNA fragments. For miR-21-5p examination, miRNA SYBR qPCR Master Mix (Vazyme, MQ101-02) was used for reverse transcription. The relative expression of genes was calculated using the $2^{-\Delta\Delta CT}$ method. The glyceraldehyde-3-phosphate dehydrogenase (*GAPDH*) or U6 was used as an internal control for mRNA or miRNA, respectively. Primer sequences are listed in Table 1.

2.6 Reactive oxygen species (ROS) level detection

2',7'-Dichlorofluorescin diacetate (DCFH-DA, Sigma-Aldrich, D6883) probe was employed to detect intracellular ROS levels [36]. Cells were stimulated with 4 μg/mL lipopolysaccharide (LPS, MCE, HY-D1056) with or without AKK-EVs for 24 h. Subsequently, intracellular ROS levels were assessed by incubating the cells with 5 μM DCFH-DA for 30 min in the dark. After washing with PBS, cells were stained with DAPI and examined by confocal microscopy. The images were observed with a fluorescence microscope (KEYENCE, BZ-X810).

2.7 Flow cytometry analysis

For macrophage polarization analysis, RAW264.7 cells were treated with 4 μg/mL LPS in the presence or absence of AKK-EVs (1×10^{10} particles/mL) for 24 h. Cells were then harvested, washed, and stained with F4/80-FITC (Biolegend, 123107) and CD86-APC (Biolegend, 105011) for 30 min in dark. After washing with PBS, the samples were analyzed by flow cytometry (CytoFLEX LX, Beckman Coulter).

2.8 Immunofluorescence staining

To evaluate macrophage polarization, RAW264.7 cells were treated with 4 μg/mL LPS in the presence or absence of AKK-EVs (1×10^{10} particles/mL) for 24 h. Cells were fixed with 4% PFA, permeabilized, and stained with anti-iNOS (Cell Signaling Technology, 13120S) or anti-Arg1 (Cell Signaling Technology, 93668S) for 12 h at 4 °C. Alexa 594-conjugated secondary antibody (Thermo Fisher, A-11007) was applied to cells and incubated for 1 h at room temperature followed by nuclear counterstaining with DAPI. Fluorescence images were acquired using a microscope (KEYENCE, BZ-X810).

2.9 Western blot analysis

Proteins were extracted from RAW264.7 or HaCaT cells using radioimmunoprecipitation (RIPA) lysis buffer (Beyotime, P0013K) according to the manufacturer's instructions. Protein concentration was determined by BCA kits (Beyotime, P0010). Equal amounts of protein were separated by SDS-PAGE and transferred to polyvinylidene fluoride (PVDF) membranes as previously described [37]. The membranes were blocked and incubated overnight at 4 °C with primary antibodies against P-P65 (Cell Signaling Technology, 3033S), P-IκBα (Proteintech, 82349-1-RR), iNOS (Cell Signaling Technology, 13120S), Arg1 (Cell Signaling Technology, 93668S), GAPDH (proteintech, 60004-1-ig). After incubation with horseradish peroxidase (HRP)-conjugated secondary antibodies, protein bands were visualized by chemiluminescence. Densitometric quantification was performed using ImageJ software, and expression levels were normalized to GAPDH.

2.10 miRNA sequencing analysis of AKK-EVs

To characterize miRNAs enriched in AKK-EVs, total RNA was isolated and miRNA libraries were prepared using the TruSeq Small RNA Sample Prep Kit (Illumina, San Diego) as previously

Table 1 Sequences of primers

Name	Forward (5'–3')	Reverse (5'–3')
Human *IL-6*	ACTCACCTCTTCAGAACGAATTG	CCATCTTTGGAAGGTTCAGGTTG
Human *IL-8*	TTTTGCCAAGGAGTGCTAAAGA	AACCCTCTGCACCCAGTTTTC
Human *TNF-α*	CCTCTCTCTAATCAGCCCTCTG	GAGGACCTGGGAGTAGATGAG
Human *TLR4*	TTGGCCCTAAACCACACAGA	TATTAGGAACCACCTCCGTGA
Human *CCL17*	GTCTTGAAGCCTCCTCACCC	GGATCTCCCTCACTGTGGCT
Human *IL-4*	GCTTCCCCCTCTGTTCTTCC	CTGCTCTGTGAGGCTGTTCA
Human *IL-33*	GGAAGAACACAGCAAGCAAAGCC	GGCCAGAGCGGAGCTTCATAAAG
Human *GAPDH*	CGGAGTCAACGGATTTGGTC	GACAAGCTTCCCGTTCTCAG
Human *FLG*	TGAAGCCTATGACACCACTGA	TCCCCTACGCTTTCTTGTCCT
Human *INL*	GCTCTGGGTTTTCTGCTTTC	GCAAGAATGTGAGCAACAGC
Mouse *Il-6*	TCTGCAAGAGACTTCCATCCAGTTGC	AGCCTCCGACTTGTGAAGTGGT
Mouse *Il-1β*	GAAATGCCACCTTTTGACAGTG	TGGATGCTCTCATCAGGACAG
Mouse *Tnf-α*	ACGTGGAACTGGCAGAAGAG	GGTTGTCTTTGAGATCCATGC
Mouse *Gapdh*	ACGGCCGCATCTTCTTGTGCA	ACGGCCAAATCCGTTCACACC

described [35]. Sequencing was performed in Illumina HiSeq2000/2500. Data processing and miRNA identification were conducted using ACGT101-miR (v4.2). Target genes were predicted using TargetScan (v5.0) and miRanda (v3.3a). Kyoto Encyclopedia of Genes and Genomes (KEGG) and Gene Ontology (GO) analyses were performed using R software packages.

2.11 Dual-luciferase reporter assay

The putative binding site of miR-21-5p on TLR4 3'UTR was predicted based on the seed region. The binding site was cloned into the PC032-pmirGLO luciferase vector. HaCaT cells were seeded into 48-well plates at a density of 1.2×10^5 cells. After an overnight incubation, cells were co-transfected with miR-21-5p mimic or mimic negative control (NC) and the constructed luciferase reporter plasmid using Lipofectamine 3000 (Thermo Fisher, L3000015). After 48 h, cells were lysed and luciferase activity was measured using the dual-luciferase reporter assay system (Promega, E1910).

2.12 *Ex vivo* stability analysis of AKK-EVs

The *ex vivo* stability of AKK-EVs was investigated as previously reported [24]. Briefly, 100 μL of AKK-EVs were mixed with 150 μL of simulated salivary fluid (Solarbio, A7990) for 5 min. The mixture was then transferred to 300 μL of simulated gastric fluid and incubated for 2 h at 37 °C under stomach-like conditions. This was followed by incubation with 300 μL of simulated intestinal fluid (small intestine-like conditions, Yuanye, R30384) for an additional 4 h, and finally with 150 μL of simulated colonic fluid for 7 h. The stability of the AKK-EVs was assessed by measuring the particle distribution and mean particle size.

2.13 *In vivo* biodistribution of AKK-EVs

AD mice and normal mice were orally administrated with 100 μL of DID-labeled AKK-EVs. Additional group of control mice received an oral gavage of 100 μL of free DID to function as the negative control. To track *in vivo* distribution after topical administration, 20 μL DID-labelled AKK-EVs were subcutaneously injected into the mouse ear skin. After 24 h, the mice were sacrificed, and major organs, including colon, ear skin, heart, liver, spleen, lungs, and kidney tissues were harvested and imaged using an IVIS Spectrum imaging system (Bruker, USA). Subsequently, ear skin and colon tissues were embedded in optimal cutting temperature (OCT) compound, frozen, and sectioned into 7-μm slices counterstained with DAPI, and images were acquired using a fluorescence microscope (KEYENCE, BZ-X810).

2.14 Animal model and treatment procedure

All experimental procedures were approved by the Institutional Animal Care and Use Committee of Shanghai University (approval number ESSHU2024-003). BALB/c mice (Male, 6–8-week-old) were purchased from Vital River Laboratory Animal Technology. Thirty mice were randomly divided into 5 groups, including normal group (Con), model group (DNFB), positive control group (dexamethasone, DEX), oral administration (PO) of AKK-EVs group (PO AKK-EVs), and subcutaneous injection (SC) of AKK-EVs group (SC AKK-EVs). 1% and 0.5% DNFB (Sigma, 70348) solutions were prepared in a 4:1 (v/v) mixture of acetone and olive oil. The AD mouse model was developed as previously reported [38] with minor modification. Briefly, on day 1, the ventral fur of the mice was removed. The next day, all mice except those in the normal control group were sensitized by topical application of 100 μL 1% DNFB to the shaved ventral skin, and further challenged by application of 20 μL of 0.4% DNFB on days 5 and 9. Since day 4, mice in the DNFB and PO AKK-EVs groups received a daily oral administration of either 100 μL of PBS or 100 μL of PBS containing AKK-EVs (1×10^{10} particles). Meanwhile, mice in the DEX group received a daily subcutaneous injection of 20 μL DEX (2.5 mg/(kg·day)) to the ear skin, while mice in the SC AKK-EVs group received 20 μL of PBS containing AKK-EVs (2×10^9 particles). Ear thickness was measured with a vernier caliper on days 1, 7 10, and 13. The mice were sacrificed on day 13, and the whole blood and ear skin samples were collected for subsequent experiments.

2.15 Evaluation of degree of dermatitis

The dermatitis score was evaluated according to previously reported [9]. Four clinical symptoms, including erythema, excoriation, dryness, and edema in the skin lesions were scored from 0 to 3, corresponding to none, mild, moderate, and severe symptoms, respectively. The severity scores were defined as the sum of these four individual scores.

2.16 Histopathology and immunohistochemistry (IHC)

Ear tissues were fixed with 4% PFA, embedded in paraffin wax and sectioned (5 μm). Hematoxylin and eosin (H&E) staining was performed to assess epidermal thickness and inflammatory cell infiltration. Mast cell infiltration was assessed using toluidine blue staining [9].

For IHC staining, tissue sections were incubated for 30 min at 75 °C, followed by deparaffinization with xylene as well as antigen retrieval with 0.01 M citrate buffer (pH 6.0) and heat with microwave oven. Subsequently, the slices were permeabilized with 0.5% TritonX-100, treated with 3% H_2O_2 to inactivate endogenous enzymes, washed with PBS, and blocked with 100% goat serum at room temperature for 1 h. Next, they were incubated with primary antibodies against anti-CD68 (Cell Signaling Technology, 97778S, 1:200) at 4 °C. After overnight incubation, the sections were processed with secondary antibody and visualized with DAB substrate. The cell nuclei were counterstained with hematoxylin. ImageJ software was used to quantify the staining.

2.17 Enzyme-linked immunosorbent assay (ELISA)

At the end of the experiment, the whole blood from mice was collected and centrifuged at 2000 rpm for 20 min to gain serum. The immunoglobulin E (IgE) level was examined using ELISA kits (eBioscience, EMIGHE) following manufacturer's instructions.

2.18 *In vivo* safety

To assess safety, mice received daily oral gavage (1×10^{10} particles in 100 μL PBS) or subcutaneous ear injection (2×10^9 particles in 20 μL PBS) of AKK-EVs for 10 days. After 24 h from the last treatment, mice were sacrificed, major organs were harvested for histological analysis by H&E staining, and blood samples were collected for standard biochemical testing.

2.19 Statistical analysis

Data are presented as mean ± standard deviation (SD) from at least three independent experiments. Statistical significance was determined using Student's t-test, one-way ANOVA, or two-way ANOVA. Values of $P < 0.05$ were considered as significant different.

3 Results

3.1 Characterization of AKK-EVs

AKK-EVs were isolated from AKK culture supernatants by differential ultracentrifugation (Fig. 1(a)). The EVs were subsequently characterized by TEM and NTA analysis to determine morphology and size traits. As expected, AKK-EVs displayed a typical spherical morphology, with a diameter ranging from 50 to 200 nm (Figs. 1(b) and 1(c))). The surface charge of AKK-EVs, as determined by dynamic light scattering, was approximately −14.63 mV (Fig. 1(d)). OmpA is a specific marker for EVs derived from Gram-negative bacteria [39]. As expected, OmpA expression was observed in AKK-EVs (Fig. 1(e)). Moreover, we analyzed the RNA and protein composition of AKK-EVs. SDS-PAGE analysis showed that the proteins in AKK-EVs were predominantly below 70 kDa (Fig. 1(f)), while agarose gel electrophoresis revealed a strong enrichment of small-molecular-weight RNAs (Fig. 1(g)). These characteristics are consistent with previously reported EVs from bacterial and mammalian cells [40–42].

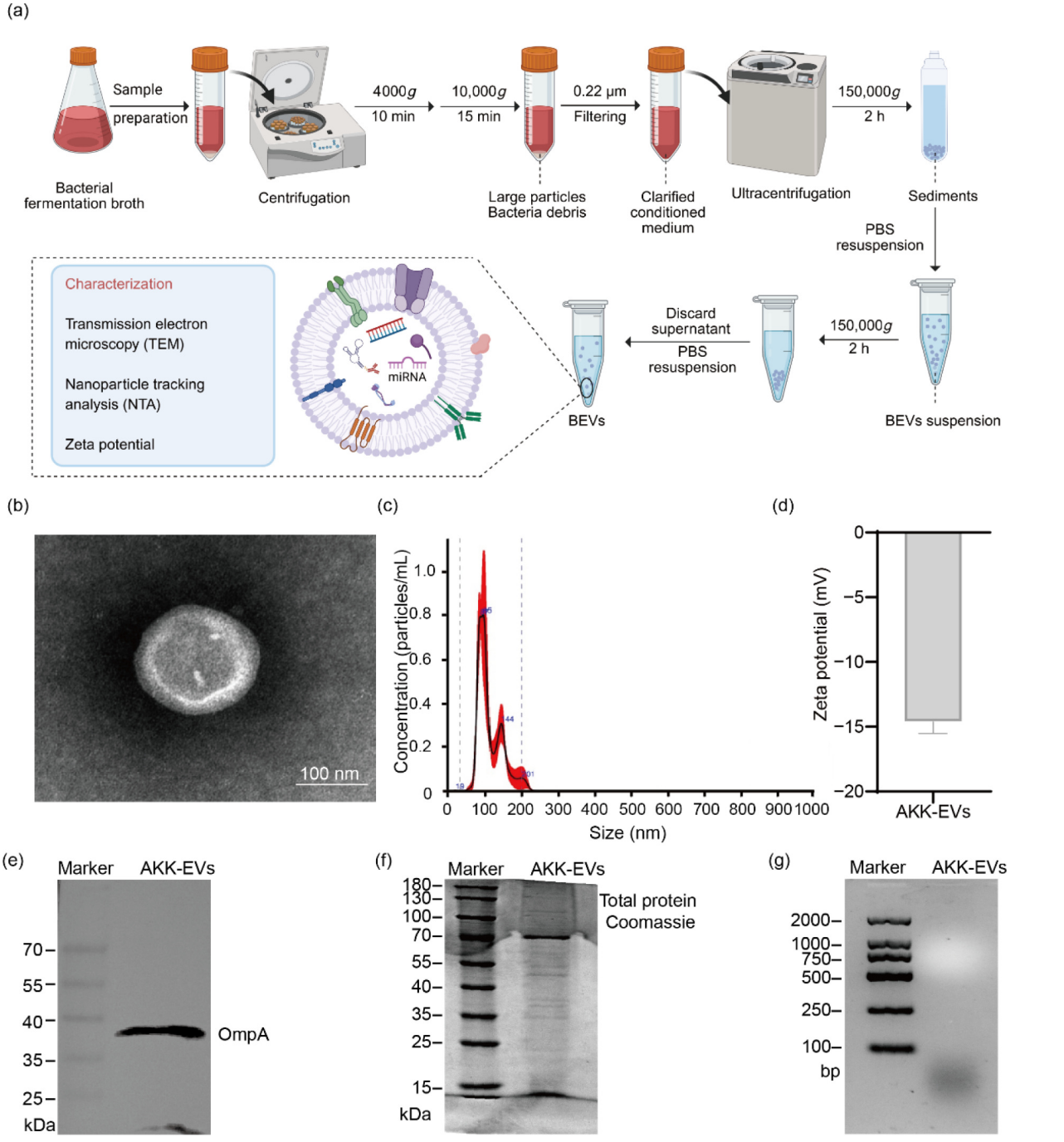

Figure 1 Characterization of AKK-EVs. (a) Schematic illustration of the isolation procedure of AKK-EVs. (b) TEM image showing the morphology of AKK-EVs. Scale bar = 100 nm. (c) NTA indicating the size distribution of AKK-EVs. (d) Quantification of the zeta potential of AKK-EVs (n = 3). Data are presented as the mean ± SD.(e) Western blot analysis of OmpA expression in AKK-EVs. (f) SDS-PAGE and Coomassie Brilliant Blue staining of total proteins in AKK-EVs. (g) Agarose gel electrophoresis analysis of RNA cargos in AKK-EVs.

3.2 Efficient internalization of AKK-EV by keratinocytes and macrophages

Because the biological functions of EVs largely depend on their uptake by recipient cells, we next examined the internalization of AKK-EVs by keratinocytes and macrophages, two key cell types involved in AD pathogenesis, via labeling them with the red fluorescent dye DID. Confocal microscopy analysis revealed that AKK-EVs were efficiently internalized by HaCaT keratinocytes and RAW264.7 macrophages in a time-dependent manner, with the uptake progressive increase over time (Figs. 2(a) and 2(b), and Figs. S1(a) and S1(b) in the Electronic Supplementary Material (ESM)). This observation indicated that AKK-EVs had the potential to transport bioactive molecules to recipient cells. Treatment with AKK-EVs at concentrations ranging from 5×10^8 to 5×10^{10} particles/mL showed no obvious cytotoxicity on both cell types, indicative of high biocompatibility (Figs. 2(c) and 2(d))). Although without statistical difference, a slight increase in keratinocyte proliferation was observed following administration with 5×10^8–5×10^9 particles/mL of AKK-EVs for 24 h. Therefore, a concentration of 1×10^{10} particles/mL was selected for subsequent experiments.

3.3 AKK-EV treatment suppresses inflammatory responses in keratinocytes and macrophages

We next examined the anti-inflammatory effects of AKK-EVs in two well-established *in vitro* models in keratinocytes, including the LPS-induced and tumor necrosis factor-α (TNF-α)/interferon-γ (IFN-γ)-induced inflammatory responses [43, 44] (Fig. 3(a), and Fig. S2(a) in the ESM). qRT-PCR analysis showed that LPS stimulation significantly upregulated the expressions of pro-inflammatory genes, including *IL-6*, *IL-8* and *TNF-α* in HaCaT cells. This upregulation was markedly reversed following treatment with AKK-EVs (Fig. 3(b)). It is well-established that TNF-α/IFN-γ synergistically drives keratinocytes to produce chemokines and inflammatory cytokines [45]. Notably, AKK-EVs attenuated TNF-α/IFN-γ-induced expression of *CCL17*, a leukocyte attracting chemokine (Fig. S2(b) in the ESM). Moreover, AKK-EVs also inhibited TNF-α/IFN-γ-induced mRNA expressions of inflammatory cytokine *IL-6* as well as Th2 inflammation associated cytokines, including *IL-4* and *IL-33* mRNA expressions in HaCaT cells (Figs. S2(c)–S2(e) in the ESM)). These inflammatory cytokines can stimulate ROS production, which in turn amplifies inflammation via a positive feedback loop, ultimately contributing to AD progression [46]. To evaluate the potential of AKK-EVs to

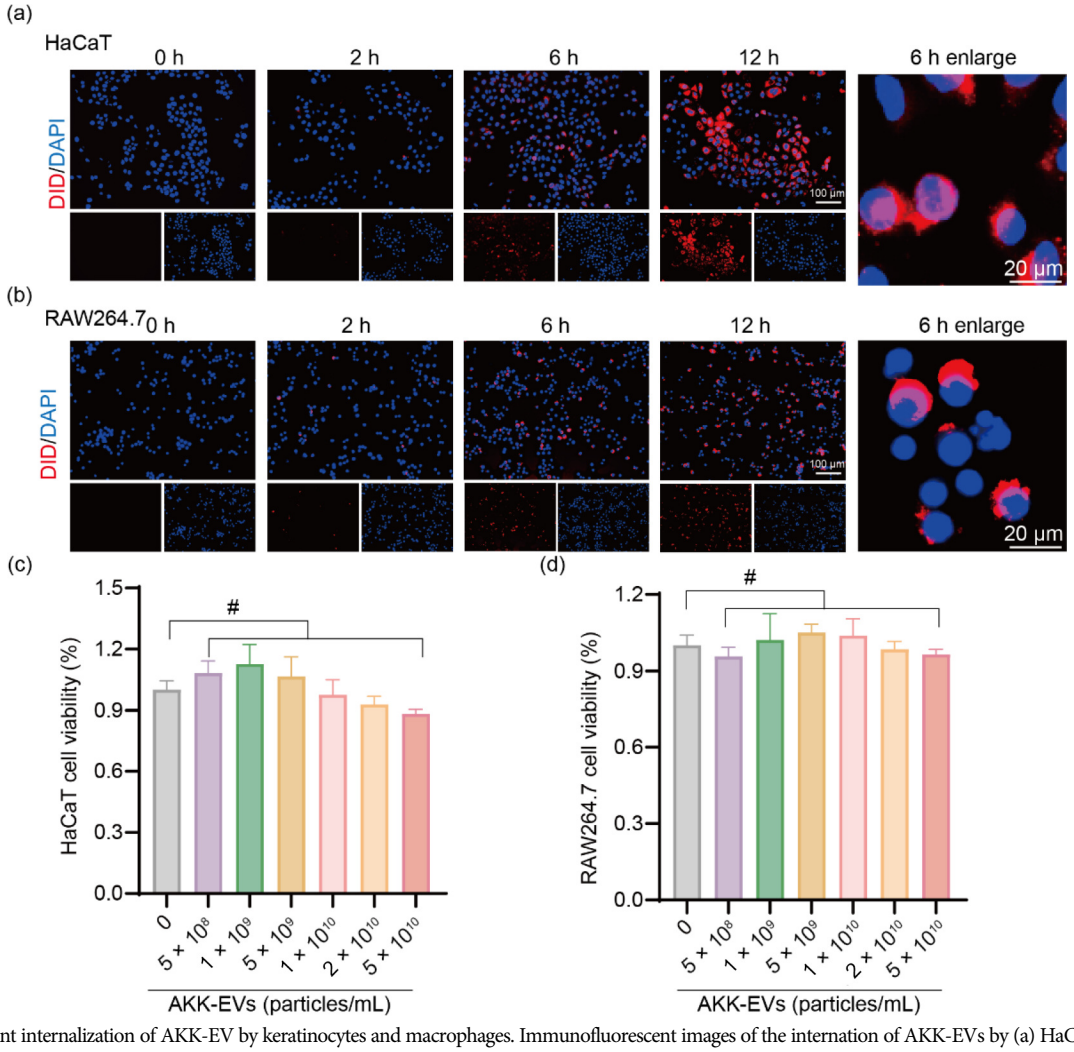

Figure 2 Efficient internalization of AKK-EV by keratinocytes and macrophages. Immunofluorescent images of the internation of AKK-EVs by (a) HaCaT keratinocytes and (b) RAW264.7 macrophages (n = 3). The DID-labeled AKK-EVs were incubated with HaCaT and RAW264.7 cells for indicated time. CCK8 analysis of the cell viability of (c) HaCaT and (d) RAW264.7 cells after treatment with various concentrations of AKK-EVs for 24 h. Data are presented as the mean ± SD; $^{\#}P > 0.05$.

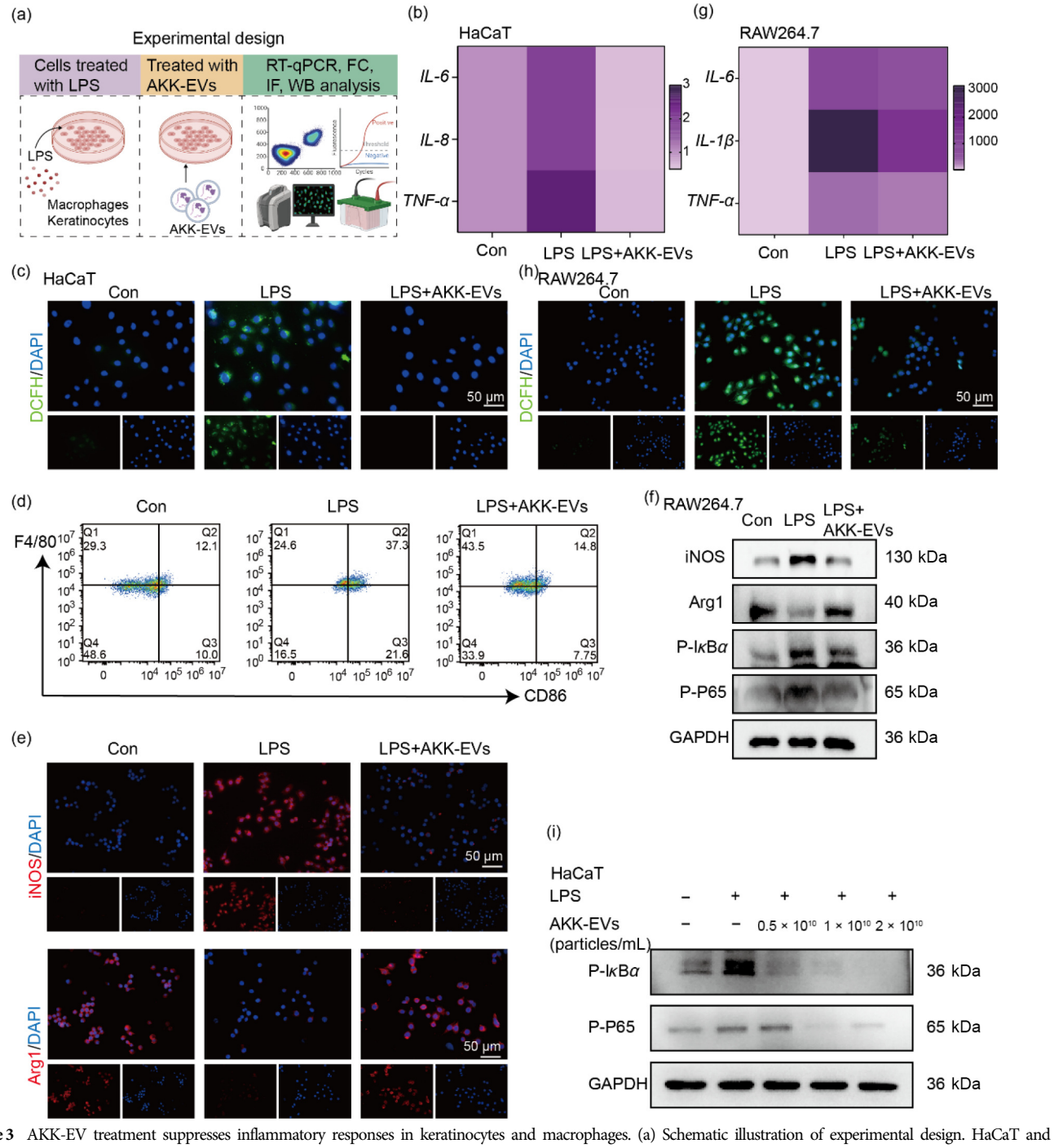

Figure 3 AKK-EV treatment suppresses inflammatory responses in keratinocytes and macrophages. (a) Schematic illustration of experimental design. HaCaT and RAW264.7 cells were treated with LPS in the presence or absence of AKK-EVs for 24 h before subsequent analysis. Heatmap showing qRT-RCR results of the pro-inflammatory gene expressions in (b) HaCaT and (g) RAW264.7 cells (n = 3). Representative immunofluorescence images showing ROS levels detected by DCFH staining in (c) HaCaT and (h) RAW264.7 cells (n = 3). (d) Flow cytometry analysis of F4/80 and CD86 expressions in RAW264.7 (n = 3). (e) Representative immunofluorescence images of iNOS and Arg1 staining in macrophages (n = 3). Western blot analysis of iNOS, Arg1, P-IκBα and P-P65 expression in (f) RAW264.7 and (i) HaCaT cells (n = 3).

counteract this oxidative stress, we assessed intracellular ROS levels using the DCFH fluorescent probe [36]. As expected, LPS robustly induced ROS production in keratinocytes, whereas treatment with AKK-EVs attenuated this increase (Fig. 3(c)). Beyond driving inflammation, TNF-α/IFN-γ signaling also contributes to skin barrier damage. We therefore investigated whether AKK-EVs could mitigate this effect. Our results showed that AKK-EVs attenuated the TNF-α/IFN-γ-induced suppression of filaggrin (FLG) and involucrin (IVL), two critical skin barrier proteins, in HaCaT cells (Fig. S3(a) in the ESM).

Macrophages exhibit high plasticity and can be polarized into pro-inflammatory M1 and anti-inflammatory M2 phenotypes. It has been reported that the AD microenvironment favors an abnormal increase in M1 macrophages and their associated inflammatory mediators [47]. Hence, we proceeded to determine the influence of AKK-EVs on macrophage polarization. LPS was

used to stimulate M1 polarization of macrophages (Fig. 3(a)). Following treatment with AKK-EVs, cells were stained with antibodies against F4/80 (a pan marker of macrophage) and CD86 (an M1-specific surface marker) and analyzed by flow cytometry. The results revealed that AKK-EVs significantly decreased the proportion of M1-like macrophages, as measured by the $F4/80^{+}CD86^{+}$ population (Fig. 3(d) and Fig. S4(a) in the ESM). Consistent with this observation, immunofluorescence staining and western blot analysis further consolidate these findings, showing that AKK-EVs obviously inhibited the expression of M1 macrophage marker inducible nitric oxide synthase (iNOS), and simultaneously promoted M2 macrophage marker Arg1 (Figs. 3(e) and 3(f), and Figs. S4(b) and S4(c) in the ESM). Correspondingly, AKK-EVs suppressed the gene expression of multiple M1-related inflammatory mediators induced by LPS, including *IL-6*, *IL-1β* and *TNF-α* (Fig. 3(g)). Furthermore, AKK-EVs also significantly attenuated LPS-induced intracellular ROS generation, as measured with fluorescence staining (Fig. 3(h)). These results support the notion that AKK-EVs polarized macrophages towards M2 state and inhibited inflammatory responses.

Next, we investigated the molecular pathways through which AKK-EVs modulate inflammation. Given that the TLR-NF-κB signaling pathway drives inflammation in AD [48], and our data showed that AKK-EVs downregulated its downstream target genes, such as *IL-6*, *IL-8*, *IL-1β* and *TNF-α*, we thus examined the influence of AKK-EVs on this pathway. In response to LPS, the inhibitory protein IκBα (nuclear factor of kappa light polypeptide gene enhancer in b-cells inhibitor, alpha) is phosphorylated and subsequently degraded, leading to the activation of the nuclear factor kappa-B (NF-κB) transcription factor (P65/P50), which translocate to the nucleus to trigger the transcription of pro-inflammatory cytokines [49]. Western blot analysis revealed that AKK-EVs treatment remarkably prevented LPS-induced NF-κB activation, as evidenced by the reduced phosphorylation of P65 (P-P65) and IκBα (P-IκBα) in HaCaT and RAW264.7 cells (Figs. 3(f) and 3(i), and Figs. S4(c) and S4(d) in the ESM). These findings suggest that AKK-EVs suppress inflammation at least in part through inhibition of the TLR-NF-κB signaling pathway.

3.4 miRNA-seq profiling of AKK-EVs

miRNAs are small noncoding RNAs that play a pivotal role in genetic regulation [50]. Since miRNAs are the most abundant functional components of EV cargos [51], we therefore focused on the miRNA contents of AKK-EVs. We performed high-throughput miRNA sequencing and identified the miRNAs through miRBase and the genome&EST. Overall, we identified 337 miRNAs, of which 168 miRNAs were novel miRNAs. The length of miRNAs in AKK-EVs mainly spanned from 18 to 23 nucleotides (Fig. 4(a)). The relative miRNA expressions were calculated via ACGT101-miR and we listed the top 10 known miRNAs with high expressions, including miR-21-5p (Fig. 4(b)). Functional enrichment analyses were conducted to predict the biological implications of these miRNAs. KEGG analysis of top 20 miRNAs revealed that they were potentially enriched in TNF signaling pathway, and inflammatory mediator regulation of TRP channels (Fig. 4(c)). In addition, we also employed GO analysis to predict the functions of these miRNAs on biological processes, cellular component and molecular function (Figs. 4(d)–4(f)). The results showed that these miRNAs were primarily enriched in biological processes related to inflammatory responses, such as NF-κB signal transduction, innate immune response, and chemotaxis (Fig. 4(d)). This finding corroborates the observed inhibitory effect of AKK-EVs on the NF-κB pathway in both macrophages and keratinocytes (Figs. 3(f) and 3(i))). Regarding cellular components, the enrichments were primarily in cell-substrate junctions, the lysosomal membrane, and tight junction (Fig. 4(e)). The enriched molecular functions were mainly associated with translation regulator activity, DNA-binding transcription factor binding, and protein serine (Fig. 4(f)). Collectively, these findings indicate that AKK-EVs carry a distinct set of miRNAs with a potential role in regulating inflammation, therefore conferring them with the therapeutic potential on AD.

3.5 miR-21-5p mediates the anti-inflammatory actions of AKK-EVs by targeting TLR4

Emerging evidence suggests BEVs-derived miRNAs can regulate mammalian cellular functions [25]. To identify the specific miRNA responsible for the anti-inflammatory effects of AKK-EVs, we focused on miR-21-5p, the most abundant miRNA detected in our sequencing dataset and hypothesized that miR-21-5p plays a pivotal role in mediating AKK-EVs-induced anti-inflammatory responses. To evaluate this, we first examined the expression of miR-21-5p in HaCaT. qRT-PCR analysis showed an increase in miR-21-5p level in HaCaT cells as early as 6 h following treatment with AKK-EVs (Fig. 5(a)). This rapid kinetic suggested that the miR-21-5p is likely derived from a pre-existing pool within AKK-EVs rather than being transcribed de novo in the recipient cells. We next determined the inhibitory effect of miR-21-5p in AKK-EVs-mediated inflammation. If this is indeed the case, the inhibition of miR-21-5p could reverse AKK-EVs actions. Therefore, we transfected the miR-21-5p inhibitor that specifically targets miR-21-5p into HaCaT cells. On miR-21-5p inhibition, AKK-EVs could not inhibit the P-IκBα and P-P65 protein levels (Fig. 5(b)). More importantly, miR-21-5p mimic decreased LPS-induced P-IκBα and P-P65 expressions (Fig. 5(b)), supporting the anti-inflammation effect of miR-21-5p. Taken together, these results suggested that AKK-EVs inhibited inflammation via miR-21-5p-mediated NF-κB inhibition.

We next investigated how miR-21-5p regulates NF-κB signaling. The TLR4/NF-κB pathway represents one of the well-known canonical NF-κB pathways that orchestrate inflammatory responses and contribute to the progression of AD [52]. Bioinformatic analysis predicted TLR4 to be a potential target gene of miR-21-5p. To validate this, we constructed TLR4-luciferase reporter plasmid containing TLR4 3'UTR binding site of miR-21-5p (Fig. 5(c)). Dual-luciferase reporter assay revealed that transfection of miR-21-5p mimic suppressed TLR4-luciferase activity compared to transfection of mimic negative control (NC) in HaCaT (Fig. 5(d)), supporting TLR4 as the direct target of miR-21-5p. Correspondingly, miR-21-5p mimic significantly decreased the expression of TLR4 on mRNA and protein level as measured with qRT-PCR and western blot, respectively in HaCaT (Figs. 5(e) and 5(f)). Meanwhile, in comparison with miR-21-5p inhibitor NC, the treatment of miR-21-5p inhibitor induced the expression of *TLR4* mRNA (Fig. 5(e)). Furthermore, the expression of downstream regulator P-P65 was also downregulated following miR-21-5p mimic treatment (Fig. 5(f)). Consistently, TLR4 expression was also significantly decreased after exposure to AKK-EVs (Fig. 5(g)). These results indicate that AKK-EVs-derived miR-21-5p serves as a

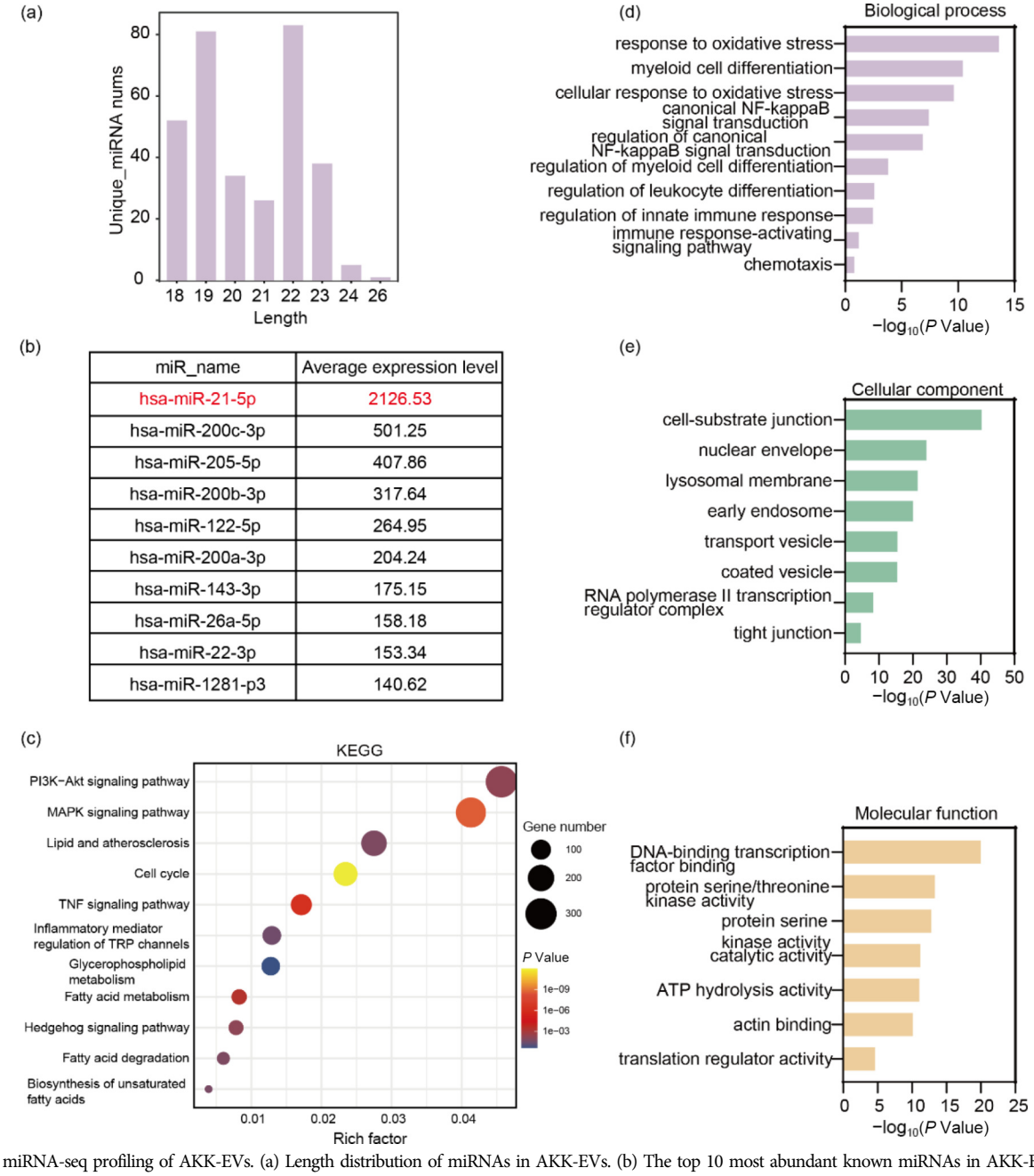

miR_name	Average expression level
hsa-miR-21-5p	2126.53
hsa-miR-200c-3p	501.25
hsa-miR-205-5p	407.86
hsa-miR-200b-3p	317.64
hsa-miR-122-5p	264.95
hsa-miR-200a-3p	204.24
hsa-miR-143-3p	175.15
hsa-miR-26a-5p	158.18
hsa-miR-22-3p	153.34
hsa-miR-1281-p3	140.62

Figure 4 miRNA-seq profiling of AKK-EVs. (a) Length distribution of miRNAs in AKK-EVs. (b) The top 10 most abundant known miRNAs in AKK-EVs (n = 3). (c) KEGG pathway enrichment analysis of the predicted target genes of top 20 miRNAs in AKK-EVs. GO analysis showing (d) the enriched biological process, (e) cellular component, and (f) molecular function of the top 20 miRNAs.

key anti-inflammatory mediator by directly binding to TLR4 and suppressing TLR4/NF-κB signaling pathway (Fig. 5(h)).

3.6 AKK-EVs exhibit excellent biosafety *in vivo*

Encouraged by the potent anti-inflammatory activity of AKK-EVs *in vitro*, we next explored biosafety *in vivo*. Mice in the SC group received a daily injection of AKK-EVs (2×10^9 particles in 20 μL PBS) via subcutaneous ear injection, while those in the PO group were orally administered (1×10^{10} particles in 100 μL PBS) once a day for 10 consecutive days. No significant weight loss was observed after AKK-EVs treatment. On day 11, major organs and blood samples were collected. H&E staining of the heart, liver, spleen, lungs, and kidneys revealed no notable histopathological abnormalities in AKK-EVs-treated mice compared to the PBS control (Con) group (Fig. 6(a)). Additionally, biochemical analysis of the serum, including the liver function indicators alanine aminotransferase (ALT) and aspartate aminotransferase (AST), as well as the kidney function parameters creatinine (CRE) and urea (UR), revealed no significant differences between the AKK-EVs treatment group and the control group (Fig. 6(b)). These results demonstrate that AKK-EVs are well tolerated and exhibit excellent systemic safety.

3.7 Stability and biodistribution of AKK-EVs after oral and topical administration

Multiple studies have demonstrated the stability of EVs in

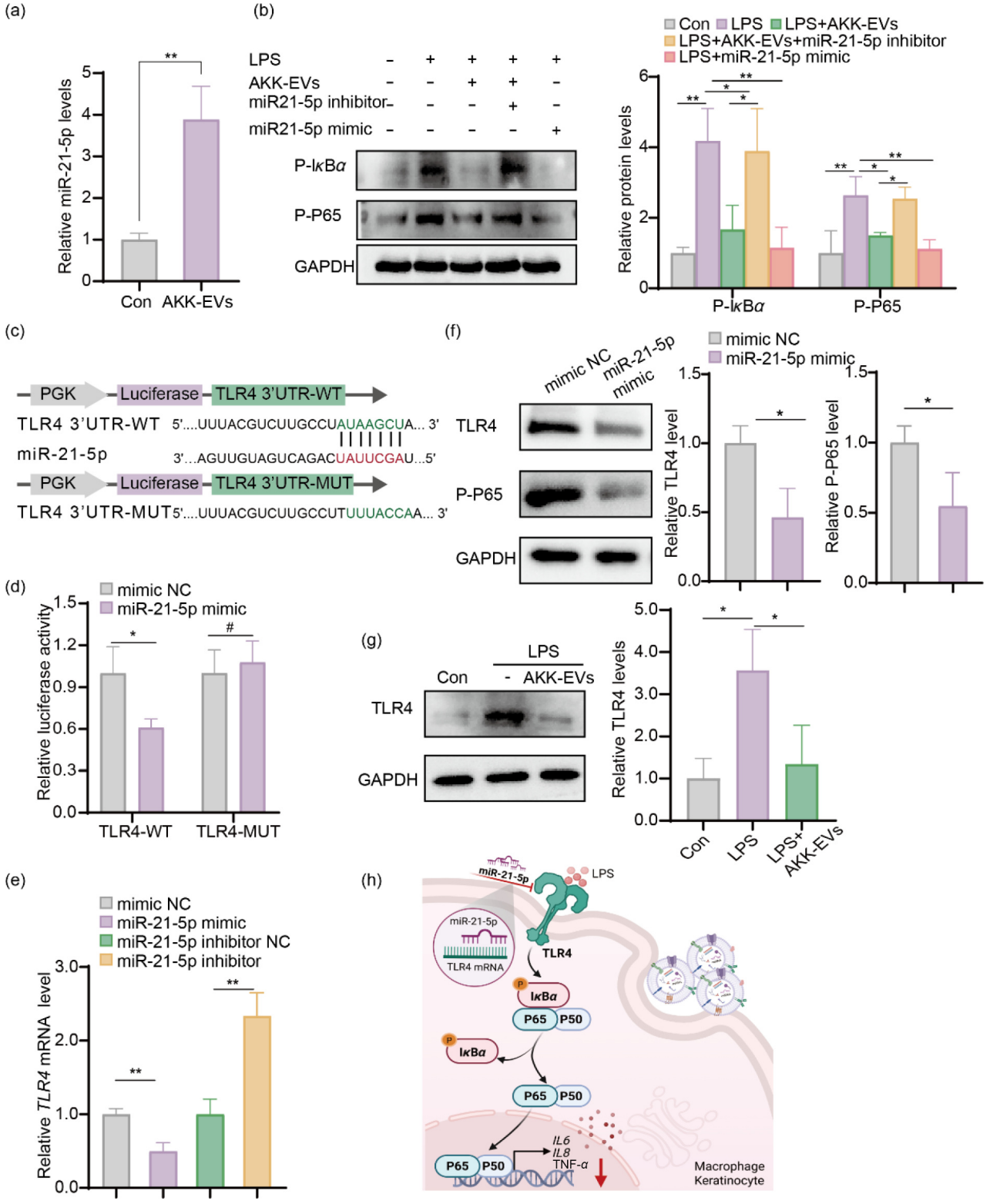

Figure 5 miR-21-5p mediates the anti-inflammatory actions of AKK-EVs via targeting TLR4. (a) qRT-PCR analysis of miR-21-5p expression in HaCaT after treatment with AKK-EVs for 6 h (n = 3). (b) Western blot analysis of P-IκBα and P-P65 expression in HaCaT. Right panel: The quantification of western blot results. After transfection of miR-21-5p inhibitor (100 nmol/L) or miR-21-5p mimic (50 nmol/L), HaCaT was treated with LPS with or without AKK-EVs (1×10^{10} particles/mL). (c) Schematic representation of the putative binding sites of miR-21-5p in the 3' UTR of TLR4. The miR-21-5p seed-matched TLR4 gene is mutated as indicated (TLR4 3' UTR-MUT). (d) Dual-reporter analysis of TLR4-luciferase activity in HaCaT cells after transfection with miR-21-5p mimic (n = 3). (e) qRT-PCR analysis of *TLR4* expression in HaCaT after transfection with miR-21-5p mimic or miR-21-5p inhibitor (n = 3). (f) Western blot analysis of the expressions of TLR4 and P-P65 in HaCaT after transfection with miR-21-5p mimic (n = 3). (g) Western blot analysis of the expression of TLR4 in HaCaT after treatment with AKK-EVs (n = 3). (h) Schematic illustration of postulated mechanism by which AKK-EVs inhibited inflammatory responses. Data are expressed as the mean ± SD. $^{\#}P > 0.05$, $^{*}P < 0.05$, $^{**}P < 0.01$, $^{***}P < 0.001$. MUT, mutant.

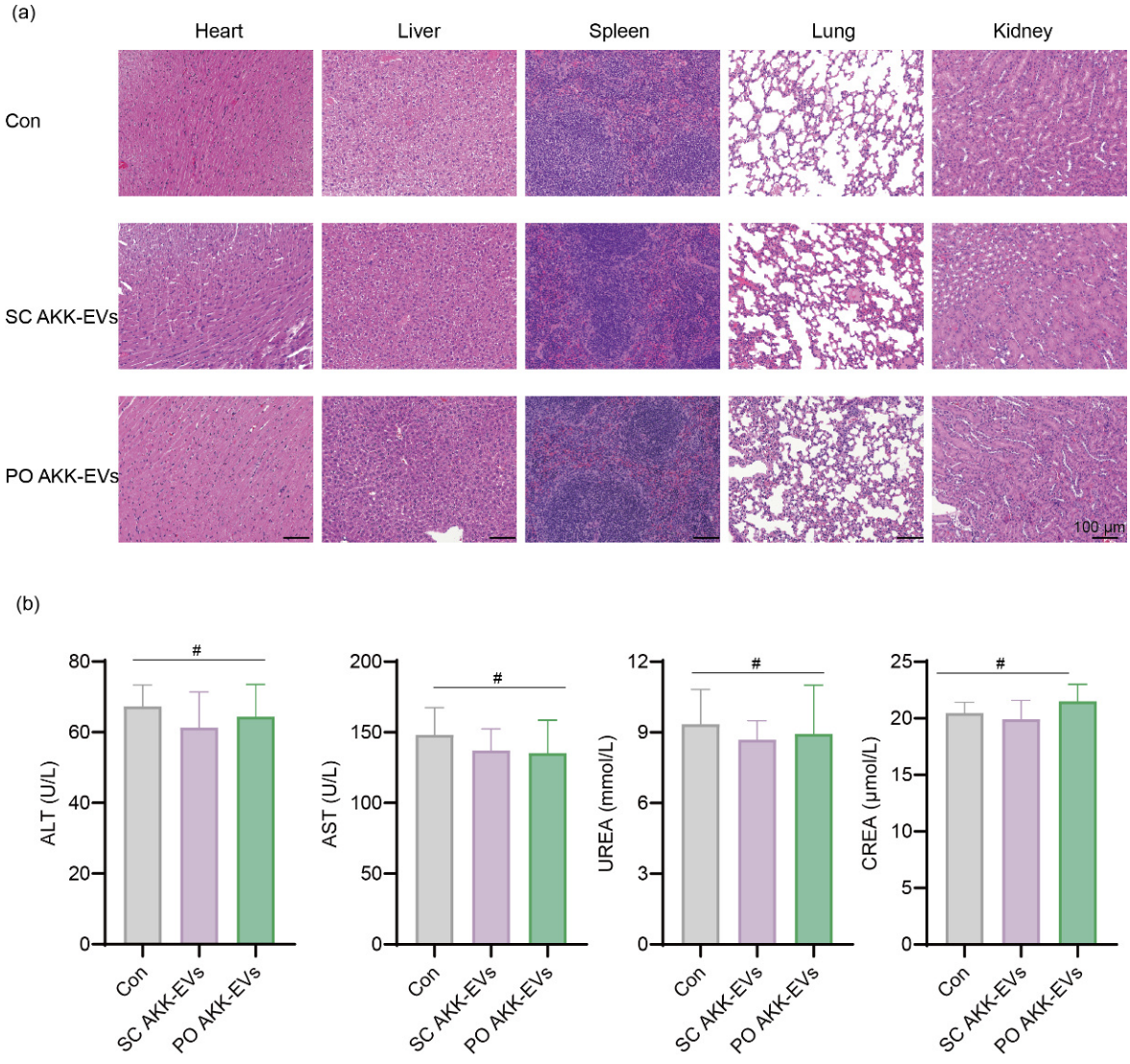

Figure 6 Safety analysis of AKK-EVs *in vivo*. (a) Representative H&E staining images of major organs from each treatment group (n = 5). (b) ALT, AST, UREA and CREA were examined by blood biochemical examination (n = 3). Data are presented as the mean ± SD. $^{\#}P > 0.05$.

biologically harsh environments, including the gastrointestinal tract [53]. Considering the high patient compliance and economical delivery route of oral administration, we sought to investigate the feasibility of oral administration of AKK-EVs. For this purpose, we first probed the gastrointestinal stability of AKK-EVs in *ex vivo* models. AKK-EVs were sequentially incubated with saliva, stimulated gastric fluid, simulated intestinal fluid, and simulated colonic fluid (Fig. 7(a)). NTA analysis showed uniform particle size distribution and mean size (Figs. 7(b) and 7(c))), indicative of favorable stability in gastrointestinal conditions. We next explored the *in vivo* distribution of DID-labeled AKK-EVs in healthy (Control) and DNFB-induced AD mice after oral gavage. *In vivo* imaging and immunofluorescence staining showed that AKK-EVs can be internalized by cells in colon both in healthy and AD mice 24 h after administration (Figs. 7(d)–7(f))). In comparison with free DID dye, more DID-labeled AKK-EVs were accumulated in colon (Figs. 7(d) and 7(e)). Notably, DID-labelled AKK-EVs concentrated prominently in the inflammatory skin lesions of DNFB-induced AD mice, indicating that AKK-EVs can cross the gastrointestinal barrier and migrate to the skin (Figs. 7(d) and 7(e)). Remarkably, DID-labeled AKK-EVs accumulated preferentially in inflamed skin lesions of DNFB-induced AD mice, but not in the skin of healthy control (Figs. 7(d)–7(f)). This may contribute to the inflammation-site targeting capability of EVs, a phenomenon also reported in other studies [24, 54]. These findings highlight the potential of AKK-EVs as a viable oral agent for AD, capable of effectively delivering bioactive cargo to the skin.

To complement these findings, we also examined the biodistribution of AKK-EVs in skin tissues following subcutaneous administration. At 24 h post-injection, fluorescence signals confirmed the presence of DID-labeled AKK-EVs in ear skin (Figs. 7(g) and 7(h)), supporting the viability of the subcutaneous route for AKK-EVs-based AD therapy. Together, these results demonstrate that AKK-EVs are highly stable in the gastrointestinal environment and can reach skin inflammatory lesions following oral administration. This dual stability and targeting capability highlight their promise as a non-invasive therapeutic platform for inflammatory skin disorders.

3.8 AKK-EVs mitigate AD symptoms *in vivo*

Having confirmed the *in vitro* biological activity, biosafety and

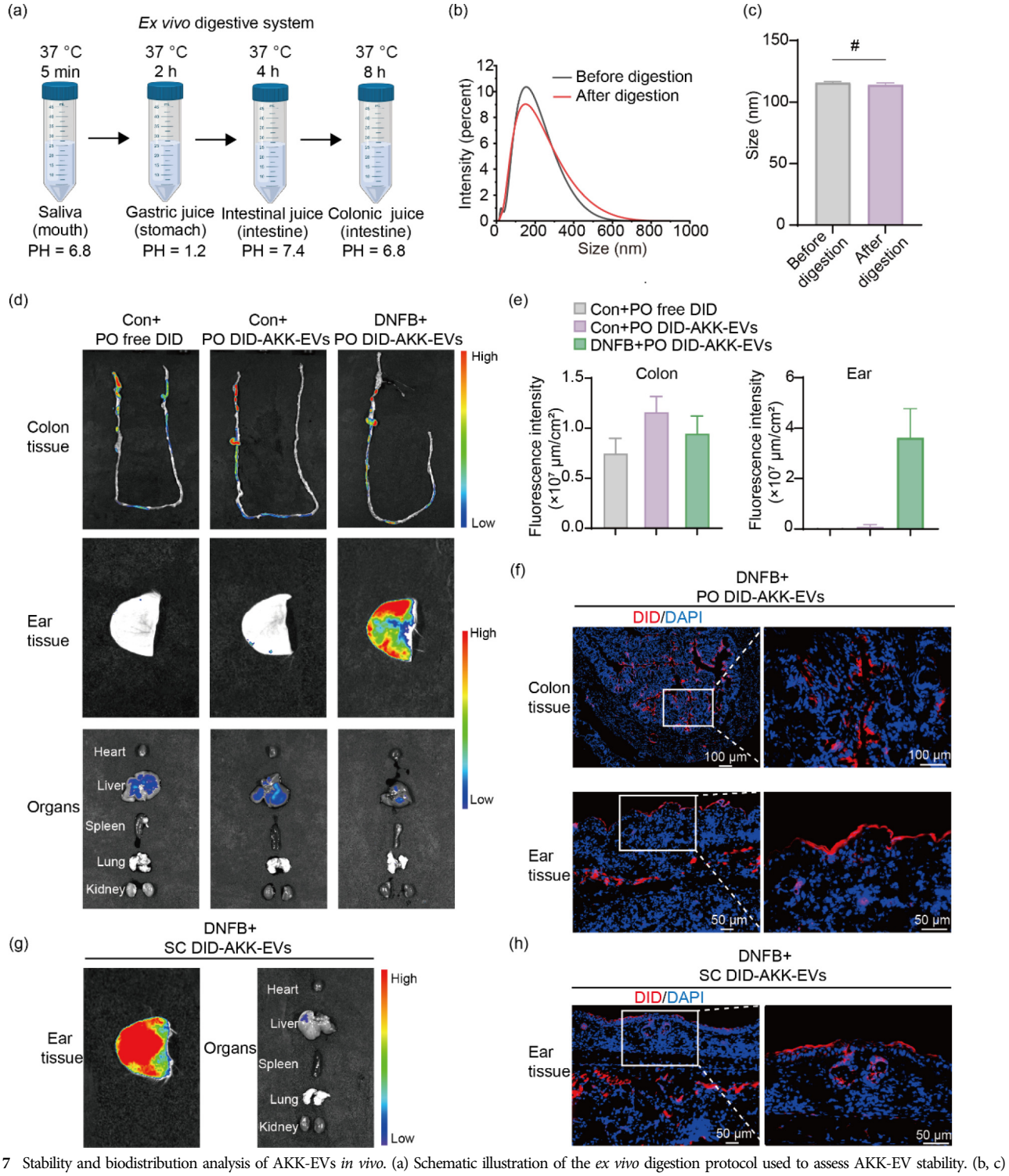

Figure 7 Stability and biodistribution analysis of AKK-EVs *in vivo*. (a) Schematic illustration of the *ex vivo* digestion protocol used to assess AKK-EV stability. (b, c) NTA analysis of (b) the size distribution and (c) mean size of AKK-EVs after *ex vivo* digestion ($n = 3$). Bio distribution analysis in healthy and DNFB-induced AD mice at 24 h after oral administration of free DID, DID-labeled AKK-EVs: (d) Representative IVIS images of major organs; (e) the quantification of relative fluorescence intensity ($n = 3$); (f) representative immunofluorescence images of colon and ear tissues from DNFB-induced AD mice after oral administration of DID-labeled AKK-EVs ($n = 3$). Biodistribution analysis in DNFB-induced AD mice at 24 h after topical administration of DID-labeled AKK-EVs: (g) Representative IVIS images of major organs ($n = 3$); (h) representative immunofluorescence images of ear tissues from DNFB-induced AD mice after topical injection of DID-labeled AKK-EVs ($n = 3$). Data are presented as the mean ± SD. $^{\#}P > 0.05$.

biodistribution of AKK-EVs, we proceeded to investigate their therapeutic potential for AD using a DNFB induced mouse model [55]. The experimental protocol was displayed in Fig. 8(a). As expected, DNFB challenge induced classical AD-like symptoms in mouse ears, including erythema, excoriation, skin thickening, dryness and weight loss (Figs. 8(b)–8(e)). Both oral and topical application of AKK-EVs effectively ameliorated these symptoms (Figs. 8(b)–8(e)). Of importance, the improvement in surface

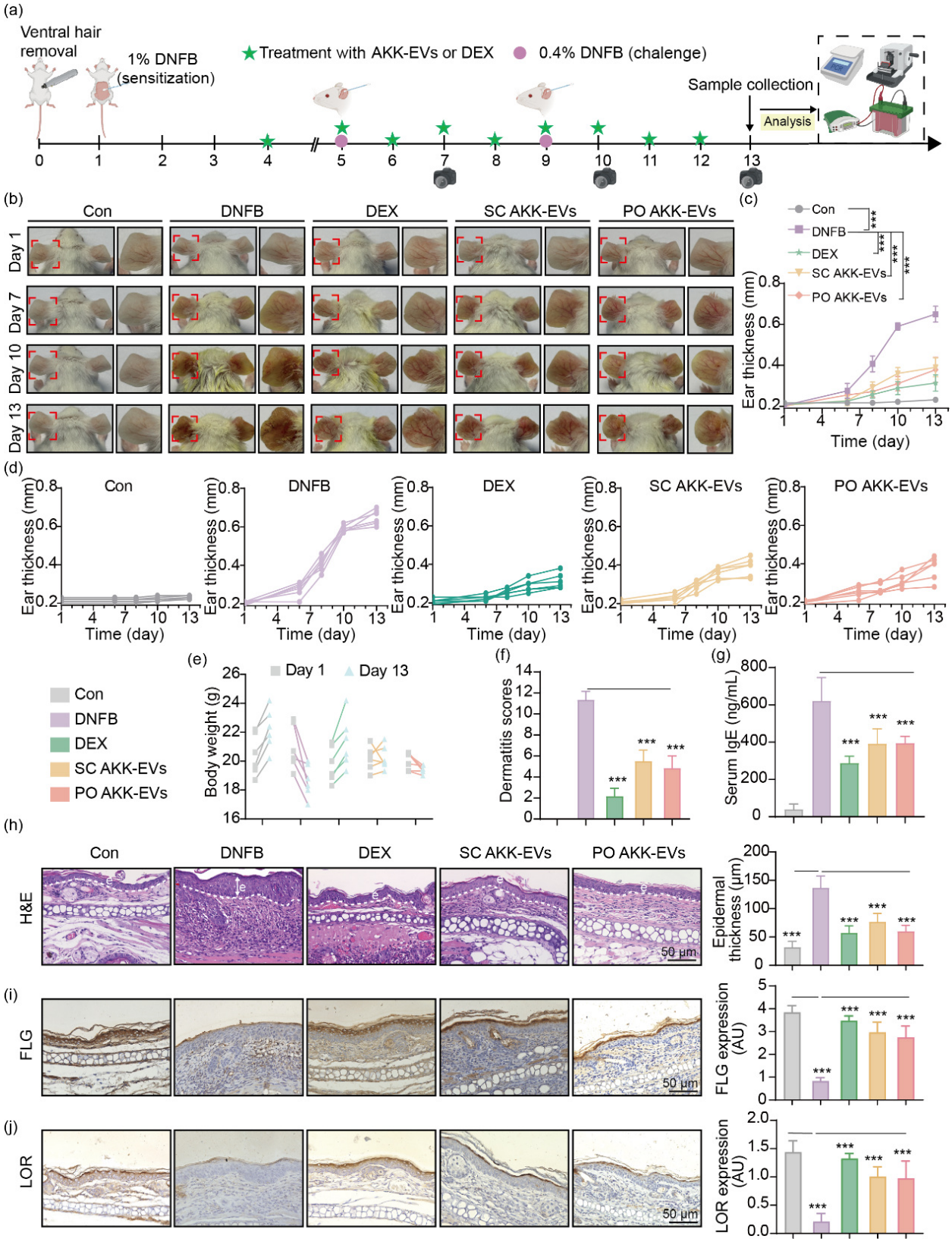

Figure 8 AKK-EVs mitigate AD symptoms *in vivo*. (a) Schematic diagram of the experimental procedure. (b) Representative images showing ear skin lesions in mice at days 1, 7, 10, and 13. (c) Dynamic changes in ear thickness over time across all groups ($n = 6$), (d) Quantitative analysis of ear thickness for each individual group. (e) Body weight of the mice was examined at days 1 and 13 ($n = 6$). (f) Dermatitis scores in skin lesions were evaluated on day 13 ($n = 6$). (g) ELISA analysis of IgE levels in serum on day 13 ($n = 5$). (h) Representative H&E staining of mouse ear tissues from different groups at the end of the experiment, and quantification of epidermal thickness ($n = 6$, right panel), "e" indicates epidermis. Representative images of IHC staining for (i) FLG and (j) LOR in mouse ear tissues from different groups at the end of the experiment ($n = 5$). Data are presented as the mean ± SD. ***$P < 0.001$.

morphology of skin lesions achieved by AKK-EVs was comparable to that of the positive control drug, DEX (Figs. 8(b)–8(d)). Additionally, the dermatitis score was reduced after AKK-EVs and DEX treatment, supporting their therapeutic potential (Fig. 8(f)). Elevated level of serum IgE is a well-established hallmark of AD severity [1]. Consistent with this, ELISA analysis confirmed a remarkable increase in serum IgE in DNFB-induced model mice. Notably, this elevation was markedly alleviated by treatment with either AKK-EVs or DEX (Fig. 8(g)). H&E staining further consolidated these findings, showing that AKK-EVs and DEX reduced epidermal hyperplasia and thickness, and dermal inflammatory cell infiltration (Fig. 8(h)).

Epidermal barrier dysfunction is a key pathogenic factor of AD [56]. Since *in vitro* finding show that AKK-EVs restored the expression of skin barrier protein (Fig. S3(a) in the ESM), we asked whether AKK-EVs could promote skin barrier repair *in vivo*. IHC staining of key skin barrier proteins, including FLG and loricrin (LOR) revealed upregulated expression by AKK-EV treatment, indicative of a restored skin barrier (Figs. 8(i) and 8(j)). These findings collectively indicate the potential of AKK-EVs to alleviate AD-like pathological abnormalities.

3.9 AKK-EVs reshape the inflammatory ecosystem in AD skin

AD involves a complex dysregulated immune response, characterized by the infiltration of proinflammatory cells and elevated levels of proinflammatory mediators, such as IL-6, IL-1β and TNF-α. To determine whether AKK-EVs modulate this immune landscape, we analyzed cellular infiltration and cytokine expression in AD lesions. The numbers of mast cells and macrophages significantly increased in DNFB-induced AD-like skin lesions. However, these pathological elevations were markedly suppressed following treatment with AKK-EVs, as demonstrated by toluidine blue staining and IHC staining against CD68, a pan-marker of macrophages (Figs. 9(a) and 9(b)). Immunofluorescence staining of macrophages in skin lesions revealed that both SC and PO administration of AKK-EVs, similar to DEX, increased the proportion of $Arg1^+$ M2 macrophages while decreasing the proportion of $iNOS^+$ M1 macrophages (Fig. 9(c)). These findings consolidated that AKK-EVs could polarize macrophages toward an anti-inflammatory phenotype. In line with this, the gene expression levels of proinflammatory mediators, including IL-6, IL-1β and TNF-α were also downregulated (Fig. 9(d)). Building on the *in vitro* confirmation of its inhibition on NF-κB signaling pathway by AKK-EVs, we assessed pathway activity *in vivo* by western blot (Figs. 9(e) and 9(f)). The results showed that AKK-EVs also inhibited the NF-κB pathway *in vivo*, as evidenced by the downregulated phosphorylation of IκBα and P65 (Figs. 9(d) and 9(e)). These results suggested that AKK-EVs exerted protective effects via suppressing NF-κB pathway *in vivo*.

4 Discussion

AD is driven by immune dysregulation and barrier defects, yet current therapies remain limited by incomplete efficacy and adverse side effects [1]. Here, we identify EVs derived from the gut commensal *AKK* as a potent, mechanistically defined regulator of AD pathology. AKK-EVs exert anti-inflammatory and antioxidant effects in keratinocytes and macrophages, and critically, deliver miR-21-5p to suppress TLR4/NF-κB signaling. *In vivo*, AKK-EVs demonstrate high stability, ameliorate AD-like skin lesions, restore barrier integrity, and reshape the local inflammatory microenvironment following both oral and subcutaneous administration (Scheme 1). Together, these findings reveal a previously unrecognized gut-skin communication pathway mediated by microbiome-derived EVs and provide a mechanistically grounded rationale for their therapeutic application in inflammatory skin disease.

Probiotic interventions have emerged as promising strategies to restore immune balance and tissue homeostasis, including chronic inflammatory skin disorders such as AD [4]. Among these, AKK stands out as a prominent probiotic with beneficial effects on inflammatory diseases [28]. For example, supplementation with AKK strains, especially in combination with probiotic *Faecalibacterium prausnitzii*, can greatly reduce AD symptoms by modulating the immune system [31], highlighting the anti-inflammatory potential of AKK. While the beneficial effects of live probiotics have been increasingly recognized, their underlying molecular mediators remain poorly defined. Recent research supports the bacteria-derived EVs as promising regulators to influence the functions of recipient cells via cross-kingdom communication [22, 57, 58]. In this study, we demonstrate that AKK-EVs exert potent anti-inflammatory effects both *in vitro* and *in vivo*, revealing that EVs may serve as critical mediators of probiotic-host communication. These findings highlight the potential of AKK-EVs as a novel, cell-free therapeutic strategy for AD.

miRNAs within EVs are key effectors in modulating recipient cell functions [51, 59]. Among these, we identified miR-21-5p as a major mediator of the anti-inflammatory activity of AKK-EVs. Exposure to AKK-EVs rapidly increased miR-21-5p levels in target cells, and functional studies confirmed its central role. Bioinformatic analysis and dual luciferase assays revealed that miR-21-5p directly targets TLR4, thereby suppressing NF-κB signaling and downstream proinflammatory cytokine production. Notably, the context-dependent nature of miR-21-5p has been reported in other systems [60, 61]. For example, Bian Z. X. et al. demonstrated that miR-21-5p blocked NF-κB signaling pathway activity in human kidney cells via an unclear mechanism [60]. In contrast, Pandey N. et al. reported that miR-21-5p promoted NF-κB activation via PTEN in human microglial cells during viral infection [61]. Our prior study revealed that miR-21-5p promoted the proliferation and migration of epithelial and endothelial cells via PI3K-AKT pathway, thereby enhancing skin wound healing [25]. In the context of AD, we found that miR-21-5p inhibited NF-κB signaling by directly targeting TLR4, which underscores the novelty of our finding within this specific inflammatory landscape. These results provide a mechanistic basis for the immunomodulatory effects of AKK-EVs and highlight the miR-21-5p/TLR4/NF-κB axis as a central pathway through which probiotic-derived EVs can ameliorate skin inflammation. Of note, while this study focused on the functional role of EVs-associated miRNAs, future work employing proteomics or DNA sequencing would be intriguing to comprehensively characterize the protein and DNA cargo of AKK-EVs, which may reveal additional mechanisms contributing to their biological effects.

Beyond their anti-inflammatory effects at molecular and cellular levels, the therapeutic potential of AKK-EVs is further supported by their favorable biodistribution and inflammation-targeting properties. We observed that orally administered AKK-EVs

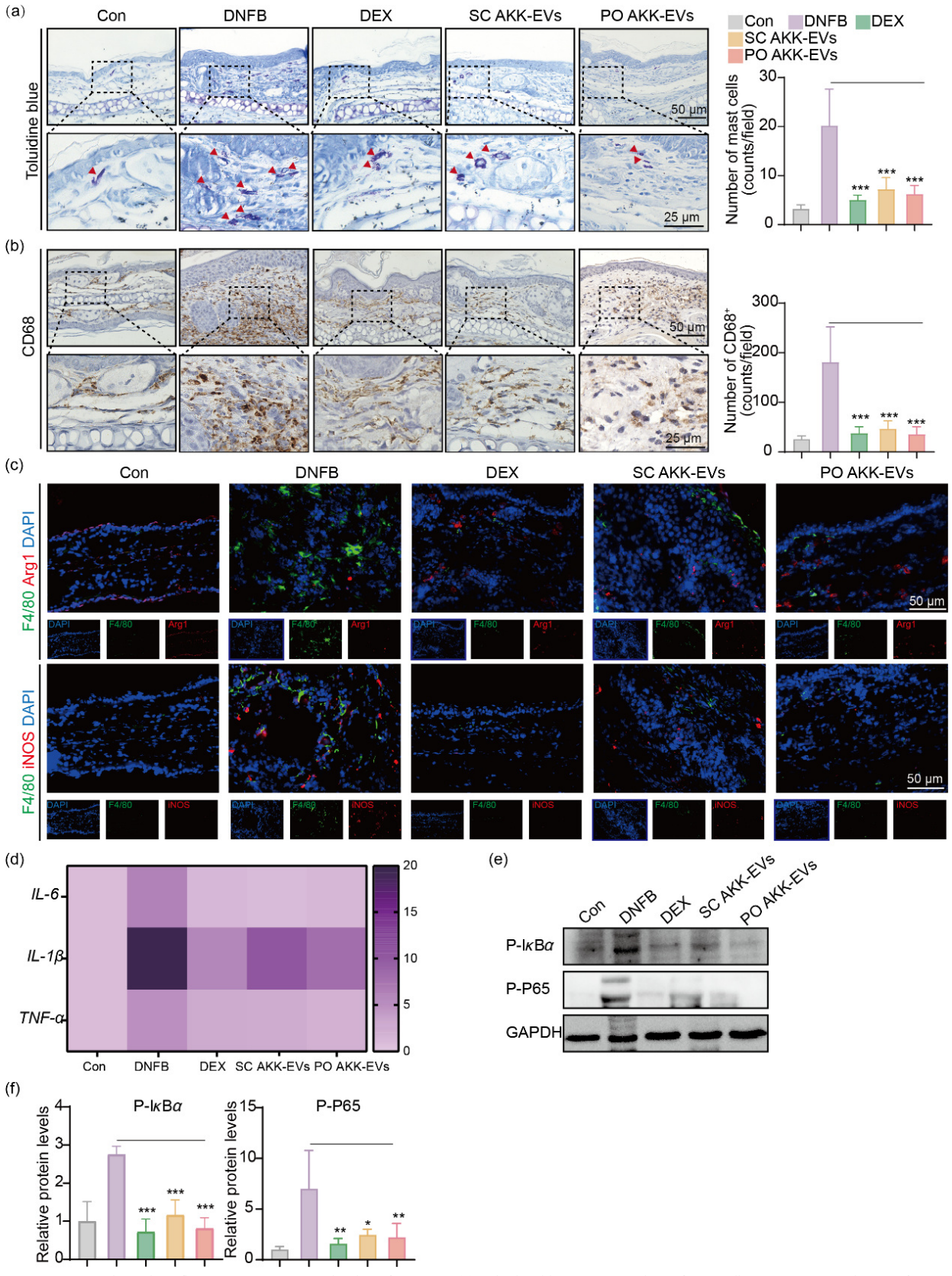

Figure 9 AKK-EVs reshape the inflammatory response in the skin of AD mice. (a) Toluidine blue staining analysis of mast cells in ear tissues, with quantification of the number of mast cells per field (n = 5). (b) Representative immunohistochemical staining of CD68 in mouse ear tissues on day 13, with quantification of the number of $CD68^+$ cells per field (n = 5). (c) Representative immunofluorescence images of iNOS, F4/80 and Arg1 staining in skin lesions (n = 4). (d) Heatmap showing the qRT-PCR analysis of pro-inflammatory gene expressions in skin lesions on day 13 (n = 4). (e) Western blot analysis of the expressions of P-IκBα and P-P65 (n = 4), with quantification shown in (f). Data are presented as the mean ± SD. $^*P < 0.05$, $^{**}P < 0.01$, $^{***}P < 0.001$.

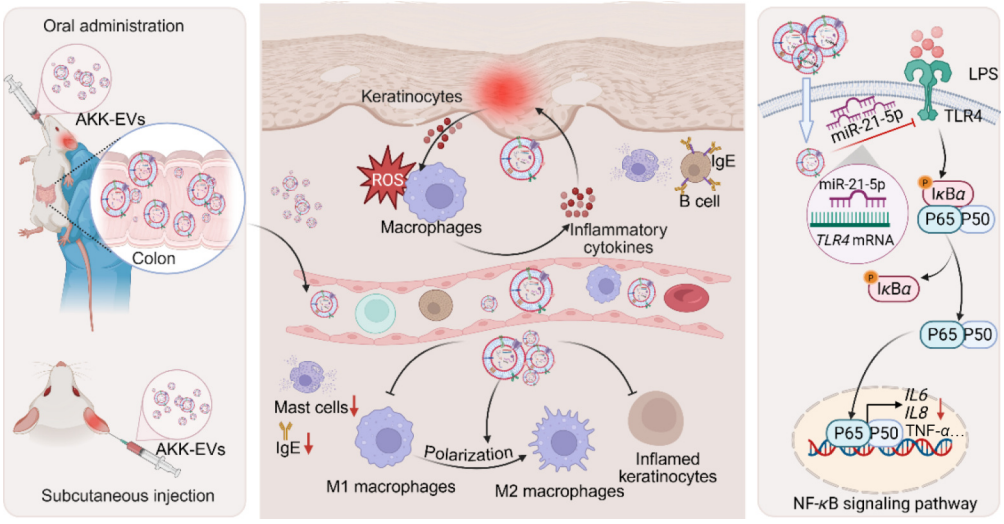

Scheme 1 Schematic illustration of AKK-EVs for AD therapy. AKK-EVs deliver miR-21-5p to mediate down-regulation of TLR4-NF-κB via gut-skin axis. Upon AKK-EVs administration, miR-21-5p is delivered to keratinocytes and macrophages, where it directly targets TLR4 and inhibits NF-κB signaling. This suppression subsequently alleviates keratinocyte inflammation and promotes macrophage polarization towards an anti-inflammatory M2 phenotype, collectively ameliorating AD symptoms. Illustration was created with BioRender.com.

remained stable throughout the gastrointestinal tract and preferentially accumulated in the colon, with remarkable enrichment at inflamed skin lesions in AD-model mice, while exhibiting minimal distribution in healthy skin. This selectively targeting likely reflects an intrinsic inflammation-homing capability, a feature increasingly recognized for certain EVs [24, 54], and highlights the potential of AKK-EVs to deliver bioactive cargo to sites of pathology in a safe and noninvasive manner. Furthermore, we demonstrated the therapeutic efficacy of AKK-EVs via subcutaneous administration, demonstrating that both oral and parenteral routes are feasible for therapeutic delivery.

In line with their targeted biodistribution, AKK-EVs exerted profound immunomodulatory effects in AD lesions. Both oral and subcutaneous administration reduced the infiltration of proinflammatory mast cells and macrophages while promoting polarization of macrophages toward an $Arg1^+$ M2 anti-inflammatory phenotype [24, 54]. This shift was accompanied by downregulation of key proinflammatory cytokines, including IL-6, IL-1β, and TNF-α, and suppression of NF-κB signaling, reinforcing the notion that AKK-EVs orchestrate a coordinated rebalancing of the inflammatory microenvironment. Beyond immune regulation, AKK-EVs also restored epidermal barrier integrity, as evidenced by upregulated expression of barrier protein in treated skin. This dual effect on inflammation and barrier function underscores the multifaceted mechanisms by which AKK-EVs ameliorate AD pathology, and highlights their potential to break the self-perpetuating cycle of barrier disruption and immune activation that characterizes chronic AD.

5 Conclusions

In conclusion, our findings propose AKK-EVs as a novel, safe, and cell-free therapeutic strategy for AD. The identified mechanism involving the delivery of miR-21-5p to inhibit the TLR4/NF-κB pathway offers a molecular level understanding of how gut bacterium remotely influence skin health. This work not only highlights the potential of AKK-EVs as a promising biotherapeutic agent but also reinforces the critical role of the gut–skin axis in inflammatory diseases. Future efforts focusing on the large-scale production and standardization of AKK-EVs will be essential to advance their clinical translation.

Electronic Supplementary Material: Supplementary material (RT-qPCR analyses of pro-inflammatory and skin barrier-associated gene expression, quantitative statistics) is available in the online version of this article at https://doi.org/10.26599/NR.2026.94908421.

Acknowledgements

This research was funded by the National Natural Science Foundation of China (Nos. 82204450, and 82272278) and the National Key Research and Development Program of China (No. 2023YFC2509000).

Data availability

The datasets used in this study are available from the corresponding author upon reasonable request.

Declaration of competing interest

The authors have declared that no competing interest exists.

Author contribution statement

J. W., X. L. D., and H. C. conceived and designed the study. Y. Y. Z., S. Q. Y., X. W. Z., J. C., and M. T. Z. performed the experiments, J. W., H. C., and Y. Y. Z. analyzed the data. J. W., H. C., and X. L. D. wrote the draft of the manuscript and critically reviewed the manuscript. H. Y. D performed the experiments. J. W., X. L. D., and Y. Y. Z. reviewed the findings and contributed to their interpretation. All authors have read and agreed to the published version of the manuscript.

Informed consent

Not applicable.

Ethics statement

All experimental procedures were approved by the Institutional Animal Care and Use Committee of Shanghai University (approval number ESSHU2024-003).

Use of AI statement

None.

References

[1] Guttman-Yassky, E.; Renert-Yuval, Y.; Brunner, P. M. Atopic dermatitis. *Lancet* **2025**, *405*, 583–596.

[2] Meledathu, S.; Naidu, M. P.; Brunner, P. M. Update on atopic dermatitis. *J. Allergy Clin. Immunol.* **2025**, *155*, 1124–1132.

[3] Bieber, T. Atopic dermatitis: An expanding therapeutic pipeline for a complex disease. *Nat. Rev. Drug Discov.* **2022**, *21*, 21–40.

[4] Suez, J.; Zmora, N.; Segal, E.; Elinav, E. The pros, cons, and many unknowns of probiotics. *Nat. Med.* **2019**, *25*, 716–729.

[5] Mahmud, M. R.; Akter, S.; Tamanna, S. K.; Mazumder, L.; Esti, I. Z.; Banerjee, S.; Akter, S.; Hasan, M. R.; Acharjee, M.; Hossain, M. S. et al. Impact of gut microbiome on skin health: Gut-skin axis observed through the lenses of therapeutics and skin diseases. *Gut Microbes* **2022**, *14*, 2096995.

[6] Jimenez-Sanchez, M.; Celiberto, L. S.; Yang, H.; Sham, H. P.; Vallance, B. A. The gut-skin axis: A bi-directional, microbiota-driven relationship with therapeutic potential. *Gut Microbes* **2025**, *17*, 2473524.

[7] Lin, X.; Yu, Z. X.; Liu, Y.; Li, C. Z.; Hu, H.; Hu, J. C.; Liu, M.; Yang, Q.; Gu, P.; Li, J. X. et al. Gut-X axis. *Imeta* **2025**, *4*, e270.

[8] Dokoshi, T.; Chen, Y.; Cavagnero, K. J.; Rahman, G.; Hakim, D.; Brinton, S.; Schwarz, H.; Brown, E. A.; O'Neill, A.; Nakamura, Y. et al. Dermal injury drives a skin to gut axis that disrupts the intestinal microbiome and intestinal immune homeostasis in mice. *Nat. Commun.* **2024**, *15*, 3009.

[9] Choi, H.; Kwak, M. J.; Choi, Y.; Kang, A. N.; Mun, D.; Eor, J. Y.; Park, M. R.; Oh, S.; Kim, Y. Extracellular vesicles of *Limosilactobacillus fermentum* SLAM216 ameliorate skin symptoms of atopic dermatitis by regulating gut microbiome on serotonin metabolism. *Gut Microbes* **2025**, *17*, 2474256.

[10] Gan, Y. Y.; Zhang, J. R.; Qi, F. F.; Grice, E. A.; Garza, L. A.; Wang, G. F. Microbial homeostasis and dysbiosis in physiological and pathological skin. *Med* **2025**, *6*, 100847.

[11] Lee, M. J.; Kang, M. J.; Lee, S. Y.; Lee, E.; Kim, K.; Won, S.; Suh, D. I.; Kim, K. W.; Sheen, Y. H.; Ahn, K. et al. Perturbations of gut microbiome genes in infants with atopic dermatitis according to feeding type. *J. Allergy Clin. Immunol.* **2018**, *141*, 1310–1319.

[12] Marrs, T.; Jo, J. H.; Perkin, M. R.; Rivett, D. W.; Witney, A. A.; Bruce, K. D.; Logan, K.; Craven, J.; Radulovic, S.; Versteeg, S. A. et al. Gut microbiota development during infancy: Impact of introducing allergenic foods. *J. Allergy Clin. Immunol.* **2021**, *147*, 613–621.e9.

[13] Liu, X. C.; Xu, J.; Wang, Z. F.; Xu, X. Q.; Wen, H.; Su, H. C.; Han, Y.; Luo, Y.; Zhang, Y.; Li, W. et al. Differential changes in the gut microbiota between extrinsic and intrinsic atopic dermatitis. *J. Autoimmun.* **2023**, *141*, 103096.

[14] Fang, Z. F.; Pan, T.; Li, L. Z.; Wang, H. C.; Zhu, J. L.; Zhang, H.; Zhao, J. X.; Chen, W.; Lu, W. W. *Bifidobacterium longum* mediated tryptophan metabolism to improve atopic dermatitis via the gut-skin axis. *Gut Microbes* **2022**, *14*, 2044723.

[15] Rios-Carlos, M.; Cervantes-García, D.; Córdova-Dávalos, L. E.; Bermúdez-Humarán, L. G.; Salinas, E. Unraveling the gut-skin axis in atopic dermatitis: Exploiting insights for therapeutic strategies. *Gut Microbes* **2024**, *16*, 2430420.

[16] Kim, W. K.; Jang, Y. J.; Han, D. H.; Jeon, K.; Lee, C.; Han, H. S.; Ko, G. *Lactobacillus paracasei* KBL382 administration attenuates atopic dermatitis by modulating immune response and gut microbiota. *Gut Microbes* **2020**, *12*, 1819156.

[17] Kim, J. H.; Kim, K.; Kim, W. Gut microbiota restoration through fecal microbiota transplantation: A new atopic dermatitis therapy. *Exp. Mol. Med.* **2021**, *53*, 907–916.

[18] Toyofuku, M.; Schild, S.; Kaparakis-Liaskos, M.; Eberl, L. Composition and functions of bacterial membrane vesicles. *Nat. Rev. Microbiol.* **2023**, *21*, 415–430.

[19] Wen, M. H.; Wang, J. Y.; Ou, Z. H.; Nie, G. J.; Chen, Y.; Li, M.; Wu, Z. W.; Xiong, S. D.; Zhou, H. W.; Yang, Z. F. et al. Bacterial extracellular vesicles: A position paper by the microbial vesicles task force of the Chinese society for extracellular vesicles. *Interdiscip. Med.* **2023**, *1*, e20230017.

[20] Liu, H.; Cheng, T.; Li, G. F.; Xia, Z. D.; Wang, C. L.; Xu, K.; Su, J. C. Organoid-tissue extracellular vesicles. *Interdiscip. Med.* **2025**, *3*, e20250006.

[21] Han, R. N.; Wu, Y.; Han, Y. F.; Liu, X. F.; Liu, H.; Su, J. C. Engineered plant extracellular vesicles for autoimmune diseases therapy. *Nano Res.* **2024**, *17*, 2857–2873.

[22] Yuan, S. Q.; Jin, M. Y.; Zhang, Y. Y.; Zhang, M. T.; Yuan, M. J.; Ding, X. L.; Wang, J. Extracellular vesicles in skin: Biological function and therapeutic potential. *Int. J. Nanomedicine* **2025**, *20*, 11211–11233.

[23] Zhang, S.; Zhang, K.; Zheng, C. X.; Gao, Y. F.; Deng, G. R.; Zhang, X.; Yuan, Y.; Jia, T.; Tang, S. Y.; He, G. X. et al. D-mannose alleviates type 2 diabetes and rescues multi-organ deteriorations by controlling release of pathological extracellular vesicles. *Exploration* **2025**, *5*, 20240133.

[24] Su, D. D.; Li, M. C.; Xie, Y. D.; Xu, Z. X.; Lv, G. W.; Jiu, Y. M.; Lin, J. X.; Chang, C. J.; Chen, H. B.; Cheng, F. Gut commensal bacteria *Parabacteroides goldsteinii*-derived outer membrane vesicles suppress skin inflammation in psoriasis. *J. Control. Release* **2025**, *377*, 127–145.

[25] Wang, J.; Li, X. J.; Zhao, X. Y.; Yuan, S. Q.; Dou, H. Y.; Cheng, T.; Huang, T. M.; Lv, Z.; Tu, Y. D.; Shi, Y. J. et al. *Lactobacillus rhamnosus GG*-derived extracellular vesicles promote wound healing via miR-21-5p-mediated re-epithelization and angiogenesis. *J. Nanobiotechnol.* **2024**, *22*, 644.

[26] Wang, J.; Yuan, S. Q.; Tu, Y. D.; Lv, Z.; Cheng, H.; Ding, X. L. Extracellular vesicles in skin health, diseases, and aging. *Interdiscip. Med.* **2024**, *2*, e20240011.

[27] Ioannou, A.; Berkhout, M. D.; Geerlings, S. Y.; Belzer, C. *Akkermansia muciniphila*: Biology, microbial ecology, host interactions and therapeutic potential. *Nat. Rev. Microbiol.* **2025**, *23*, 162–177.

[28] Cani, P. D.; Depommier, C.; Derrien, M.; Everard, A.; de Vos, W. M. *Akkermansia muciniphila*: Paradigm for next-generation beneficial microorganisms. *Nat. Rev. Gastroenterol. Hepatol.* **2022**, *19*, 625–637.

[29] Sasaki, M.; Schwab, C.; Ramirez Garcia, A.; Li, Q.; Ferstl, R.; Bersuch, E.; Akdis, C. A.; Lauener, R.; Frei, R.; Roduit, C. The abundance of *Ruminococcus bromii* is associated with faecal butyrate levels and atopic dermatitis in infancy. *Allergy* **2022**, *77*, 3629–3640.

[30] Plovier, H.; Everard, A.; Druart, C.; Depommier, C.; Van Hul, M.; Geurts, L.; Chilloux, J.; Ottman, N.; Duparc, T.; Lichtenstein, L. et al. A purified membrane protein from Akkermansia muciniphila or the pasteurized bacterium improves metabolism in obese and diabetic mice. *Nat. Med.* **2017**, *23*, 107–113.

[31] Lee, Y.; Byeon, H. R.; Jang, S. Y.; Hong, M. G.; Kim, D.; Lee, D.; Shin, J. H.; Kim, Y.; Kang, S. G.; Seo, J. G. Oral administration of *Faecalibacterium prausnitzii* and *Akkermansia muciniphila* strains from humans improves atopic dermatitis symptoms in DNCB induced NC/Nga mice. *Sci. Rep.* **2022**, *12*, 7324.

[32] Liu, J. H.; Chen, C. Y.; Liu, Z. Z.; Luo, Z. W.; Rao, S. S.; Jin, L.; Wan, T. F.; Yue, T.; Tan, Y. J.; Yin, H. et al. Extracellular vesicles from child gut microbiota enter into bone to preserve bone mass and strength. *Adv. Sci.* **2021**, *8*, 2004831.

[33] Liu, H.; Zhang, H.; Han, Y. F.; Hu, Y.; Geng, Z.; Su, J. C. Bacterial

extracellular vesicles-based therapeutic strategies for bone and soft tissue tumors therapy. *Theranostics* **2022**, *12*, 6576–6594.
[34] Welsh, J. A.; Goberdhan, D. C. I.; O'Driscoll, L.; Buzas, E. I.; Blenkiron, C.; Bussolati, B.; Cai, H. J.; Di Vizio, D.; Driedonks, T. A. P.; Erdbrügger, U. et al. Minimal information for studies of extracellular vesicles (MISEV2023): From basic to advanced approaches. *J. Extracell. Vesicles* **2024**, *13*, e12404.
[35] Liu, H.; Wu, Y.; Wang, F. X.; Wang, S. C.; Ji, N.; Wang, M. K.; Zhou, G. Y.; Han, R. N.; Liu, X. R.; Weng, W. Z. et al. Bone-targeted engineered bacterial extracellular vesicles delivering miRNA to treat osteoporosis. *Compos. Part B: Eng.* **2023**, *267*, 111047.
[36] Du, Y. J.; Huo, Y.; Yang, Q.; Han, Z. H.; Hou, L. Q.; Cui, B. X.; Fan, K.; Qiu, Y. K.; Chen, Z.; Huang, W. P. et al. Ultrasmall iron-gallic acid coordination polymer nanodots with antioxidative neuroprotection for PET/MR imaging-guided ischemia stroke therapy. *Exploration* **2023**, *3*, 20220041.
[37] Kong, Y.; Zhao, X. Y.; Wang, Z. F.; Yuan, S. Q.; Chen, S.; Lou, S. D.; Ma, S. C.; Li, Y. F.; Wang, X. H.; Ge, Y. F. et al. A selective fibroblast growth factor receptor 1/2 PROTAC degrader with antitumor activity. *Mol. Cancer Ther.*, in press, DOI: 10.1158/1535-7163.MCT-23-0719.
[38] Wang, Y. J.; Tan, L. X.; Jiao, K. J.; Xue, C.; Tang, Q. L.; Jiang, S.; Ren, Y. N.; Chen, H.; El-Aziz, T. M. A.; Abdelazeem, K. N. M. et al. Scutellarein attenuates atopic dermatitis by selectively inhibiting transient receptor potential vanilloid 3 channels. *Br. J. Pharmacol.* **2022**, *179*, 4792–4808.
[39] Chen, Y.; Ou, Z. H.; Pang, M. L.; Tao, Z. X.; Zheng, X. F.; Huang, Z. P.; Wen, D. N.; Li, Q. B.; Zhou, R. S.; Chen, P. et al. Extracellular vesicles derived from *Akkermansia muciniphila* promote placentation and mitigate preeclampsia in a mouse model. *J. Extracell. Vesicles* **2023**, *12*, e12328.
[40] Chen, Y.; Huang, X. Y.; Liu, A. Q.; Fan, S. Y.; Liu, S. Y.; Li, Z. H.; Yang, X. X.; Guo, H.; Wu, M. L.; Liu, M. et al. *Lactobacillus reuteri* vesicles regulate mitochondrial function of macrophages to promote mucosal and cutaneous wound healing. *Adv. Sci.* **2024**, *11*, 2309725.
[41] Liu, H.; Song, P. R.; Zhang, H.; Zhou, F. J.; Ji, N.; Wang, M. K.; Zhou, G. Y.; Han, R. N.; Liu, X. R.; Weng, W. Z. et al. Synthetic biology-based bacterial extracellular vesicles displaying BMP-2 and CXCR4 to ameliorate osteoporosis. *J. Extracell. Vesicles* **2024**, *13*, e12429.
[42] Song, Y. L.; You, Y. C.; Xu, X. Y.; Lu, J. Y.; Huang, X. J.; Zhang, J. C.; Zhu, L. W.; Hu, J. H.; Wu, X. C.; Xu, X. L. et al. Adipose-derived mesenchymal stem cell-derived exosomes biopotentiated extracellular matrix hydrogels accelerate diabetic wound healing and skin regeneration. *Adv. Sci.* **2023**, *10*, 2304023.
[43] Huang, R. F.; Jia, B.; Su, D. D.; Li, M. C.; Xu, Z. X.; He, C.; Huang, Y. S.; Fan, H.; Chen, H. B.; Cheng, F. Plant exosomes fused with engineered mesenchymal stem cell-derived nanovesicles for synergistic therapy of autoimmune skin disorders. *J. Extracell. Vesicles* **2023**, *12*, e12361.
[44] Shin, K. O.; Lee, J. H.; Chae, S.; Goto, K.; An, H.; Wakefield, J. S.; Ha, D. H.; Lee, H.; Lee, K.; Lee, H. et al. Small EVs from adipose-derived MSCs modulate epidermal barrier and inflammation via sphingosine-1-phosphate signaling pathway. *J. Extracell. Vesicles* **2025**, *14*, e70121.
[45] Kwon, Y.; Kang, Y. J.; Kwon, J.; Cho, S. Y.; Kim, J.; Le, T. T.; Hwang, H.; Deshar, B.; Kim, M.; Kim, J. Y. et al. *Forsythia velutina* Nakai extract: A promising therapeutic option for atopic dermatitis through multiple cell type modulation. *Allergy* **2024**, *79*, 1242–1257.
[46] Bertino, L.; Guarneri, F.; Cannavò, S. P.; Casciaro, M.; Pioggia, G.; Gangemi, S. Oxidative stress and atopic dermatitis. *Antioxidants* **2020**, *9*, 196.
[47] Yang, L.; Fu, J. R.; Han, X.; Zhang, C. Y.; Xia, L.; Zhu, R. H.; Huang, S. H.; Xiao, W. F.; Yu, H. M.; Gao, Y. J. et al. *Hsa_circ_0004287* inhibits macrophage-mediated inflammation in an N^6-methyladenosine-dependent manner in atopic dermatitis and psoriasis. *J. Allergy Clin. Immunol.* **2022**, *149*, 2021–2033.
[48] Han, J.; Cai, X. Y.; Qin, S. C.; Zhang, Z. Y. O.; Wu, Y. Y.; Shi, Y. Z.; Deng, T. Y.; Chen, B. J.; Liu, L.; Qian, H. S. et al. *TMEM232* promotes the inflammatory response in atopic dermatitis via the nuclear factor-κB and signal transducer and activator of transcription 3 signalling pathways. *Br. J. Dermatol.* **2023**, *189*, 195–209
[49] Guo, Q.; Jin, Y. Z.; Chen, X. Y.; Ye, X. M.; Shen, X.; Lin, M. X.; Zeng, C.; Zhou, T.; Zhang, J. NF-κB in biology and targeted therapy: New insights and translational implications. *Sig. Transduct. Target. Ther.* **2024**, *9*, 53.
[50] Diener, C.; Keller, A.; Meese, E. Emerging concepts of miRNA therapeutics: From cells to clinic. *Trends Genet.* **2022**, *38*, 613–626.
[51] Isaac, R.; Reis, F. C. G.; Ying, W.; Olefsky, J. M. Exosomes as mediators of intercellular crosstalk in metabolism. *Cell Metab.* **2021**, *33*, 1744–1762.
[52] Shi, J. R.; He, L.; Tao, R.; Zheng, H. W.; Li, W.; Huang, S. S.; Li, Y. L.; Shang, S. Q. *TLR4* polymorphisms as potential predictors of atopic dermatitis in Chinese Han children. *J. Clin. Lab. Anal.* **2022**, *36*, e24385.
[53] Gao, B. W.; Huang, X. L.; Fu, J. L.; Chen, L. Y.; Deng, Z. C.; Wang, S. H.; Zhu, Y. Y.; Xu, C. X.; Zhang, Y. J.; Zhang, M. X. et al. Oral administration of *Momordica charantia*-derived extracellular vesicles alleviates ulcerative colitis through comprehensive renovation of the intestinal microenvironment. *J. Nanobiotechnol.* **2025**, *23*, 261.
[54] Liu, C.; Yan, X. J.; Zhang, Y. J.; Yang, M.; Ma, Y. N.; Zhang, Y. Y.; Xu, Q. R.; Tu, K. S.; Zhang, M. Z. Oral administration of turmeric-derived exosome-like nanovesicles with anti-inflammatory and pro-resolving bioactions for murine colitis therapy. *J. Nanobiotechnol.* **2022**, *20*, 206.
[55] Yue, C. C.; Hu, Y. W.; Yu, J. D.; Zhou, H.; Zhou, P.; Hu, J.; Wang, X. Y.; Gu, L. N.; Li, Y.; Feng, Y. T. et al. IL-38 aggravates atopic dermatitis via facilitating migration of langerhans cells. *Int. J. Biol. Sci.* **2024**, *20*, 3094–3112.
[56] You, H. Y.; Liang, Y. S. Atopic dermatitis: The relationship between immune mediators and skin lipid barrier. *Clin. Rev. Allergy Immunol.* **2025**, *68*, 49.
[57] Dagnelie, M. A.; Corvec, S.; Khammari, A.; Dréno, B. Bacterial extracellular vesicles: A new way to decipher host-microbiota communications in inflammatory dermatoses. *Exp. Dermatol.* **2020**, *29*, 22–28.
[58] Han, F.; Wang, K. J.; Shen, K.; Wang, J.; Han, S. C.; Hu, D. H.; Wu, G. F. Extracellular vesicles from *Lactobacillus druckerii* inhibit hypertrophic scar fibrosis. *J. Nanobiotechnol.* **2023**, *21*, 113.
[59] Hu, S. Q.; Li, Z. H.; Lutz, H.; Huang, K.; Su, T.; Cores, J.; Dinh, P. U. C.; Cheng, K. Dermal exosomes containing miR-218-5p promote hair regeneration by regulating β-catenin signaling. *Sci. Adv.* **2020**, *6*, eaba1685.
[60] Bian, Z. X.; Wang, X. X.; Zhu, R.; Chen, S. J. miR-21-5p in extracellular vesicles obtained from adipose tissue-derived stromal cells facilitates tubular epithelial cell repair in acute kidney injury. *Cytotherapy* **2023**, *25*, 310–322
[61] Pandey, N.; Rastogi, M.; Singh, S. K. Chandipura virus dysregulates the expression of hsa-miR-21-5p to activate NF–κB in human microglial cells. *J. Biomed. Sci.* **2021**, *28*, 52.